10. Photoemission Electron Microscopy

Jun Feng, Andreas Scholl

Photoemission electron microscopy (PEEM) is a cathode lens electron microscopy technique. This specialized electron microscopy technique excels in studying the morphology, electronic and chemical properties and the magnetic structure of surfaces and thin film materials with nanometer-scale spatial resolution. In this chapter, we describe X-PEEM instrumentation and a typical X-PEEM optical system, discuss aberrations that limit the optical performance of X-PEEM microscopes, describe contrast mechanisms, and present several examples that cover some of the common use cases for X-PEEM, in particular the magnetic and time-resolved microscopy of nanostructures.

10.1 A Brief History of PEEM

Photoemission electron microscopy (PEEM) and the closely related low-energy electron microscopy (LEEM) technique are types of cathode lens microscopies that are widely used in materials sciences, surface chemistry, and magnetism research [10.1]. This chapter focuses in particular on x-ray PEEM and complements the chapters on PEEM, LEEM, and electron-optical design by R. Tromp and E. Bauer. In PEEM, ultraviolet (UV) light or x-rays that hit a material will release photoelectrons from the surface [10.2]. The photoemission electron microscope forms an image by projecting these electrons onto a two-dimensional detector. The invention of photoemission electron microscopy dates to the early 1930s, shortly after the introduction of electron lenses. The first working photoemission electron microscope was built by *Brüche* in 1932 [10.3, 4]. UV light from a mercury lamp was focused by a quartz lens onto the sample, which acted as the electron-emitting cathode. The electrons were then accelerated by a large electric field between the sample and the anode and projected onto a phosphor screen. At about the same time, *Knoll* et al. constructed an emission microscope using two magnetic lenses [10.5]. The first calculation of the resolution in emission microscopy was published by *Langmuir* in 1937 [10.6], and subsequent treatments were published by *Recknagel* [10.7]. PEEM techniques

P.W. Hawkes, J.C.H. Spence (Eds.), *Springer Handbook of Microscopy*, Springer Handbooks,
https://doi.org/10.1007/978-3-030-00069-1_10

were refined and improved by *Engel* [10.8]. Engel's PEEM achieved an order-of-magnitude increase in spatial resolution over previous instruments and served as a prototype for the KE-3 emission microscopes developed by *Wegmann* in the 1970s [10.9]. At this time, it was recognized that PEEM is a surface technique, which requires proper attention to the condition of the sample surface on an atomic scale [10.8, 10]. A detailed description of the early history of electron lenses and electron microscopy can be found in [10.11, 12].

In the development of PEEM, the Oregon microscope project played an important role. Led by *Griffith* and *Rempfer*, the group developed and built an ultra-high vacuum UV-PEEM that reached a spatial resolution of 10 nm and was used for the imaging of biological samples [10.10, 13]. *Rempfer* also investigated the aberrations that limit the spatial resolution of PEEM and of electron lenses, both in experiment and in theory [10.14, 15]. In the 1980s, *Telieps* and *Bauer* developed an electron microscope with both LEEM and PEEM modes [10.16]. Instead of photoelectrons, LEEM employs electron diffraction of low-energy electrons from an electron gun and excels in the investigation of crystalline surfaces, epitaxial films, and film growth. This research led to the development of SPELEEM, an instrument that combined spectroscopic photoelectron and electron diffraction imaging [10.17].

A relatively recent development is the use of x-rays instead of UV radiation. X-ray photoemission electron microscopy (X-PEEM) was introduced as a new technique in 1988 by *Tonner* and *Harp* [10.18]. In 1993, *Stöhr* et al. demonstrated that X-PEEM is capable of imaging magnetic domains at high resolution, which has become a key application of X-PEEM [10.19]. X-PEEM instrumentation has evolved rapidly during the last two decades, and many synchrotron x-ray sources use the PEEM instrument [10.20–33].

Aberration correction is a relatively recent development in the field of immersion lens microscopy. PEEM and, especially, X-PEEM microscopes are limited in resolution to typically several tens of nanometers by the chromatic and spherical aberrations of the electron lenses and the accelerating field. Based on the pioneering work by *Haider* and *Rose* et al. for transmission electron microscopes (TEM) [10.34] and *Rempfer* et al. for PEEM [10.35], several groups have developed aberration-corrected microscopes that are designed to reach low nanometer resolution [10.26, 35–40].

In Sect. 10.2, we will discuss the basic layout of an X-PEEM setup. We will describe the image generation due to x-ray absorption and discuss basic contrast mechanisms. Section 10.3 will describe the electron optics of non-aberration-corrected PEEM microscopes, and the following Sect. 10.4 will extend the discussion to aberration correction. Section 10.5 will provide several examples highlighting X-PEEM as a prototypical x-ray spectromicroscopy technique. We will, in particular, discuss x-ray dichroism imaging, which has found wide application as a magnetic domain imaging method. Section 10.6 will introduce time-resolved X-PEEM imaging, which has been developed to image magnetization dynamics with picosecond time resolution.

10.2 X-Ray PEEM

10.2.1 X-Ray Sources

Electron storage rings, also called synchrotrons, are today's premier sources of high-brightness, quasi-constant-wave x-ray beams, also called synchrotron radiation. Such a high-brightness x-ray beam is tightly collimated and can be easily focused into a micron-size spot. Synchrotron radiation is generated when relativistic charged particles—at x-ray user facilities usually electrons—are deflected, for example, by a dipole bending magnet or by a periodic magnetic structure, called a *wiggler* or *undulator*. Depending on the type of the source and the energy of the electron beam, a wide range of wavelengths, from micrometers (infrared) to angstroms (hard x-rays), and energies, from millielectronvolts to kiloelectronvolts, are produced [10.41].

Most X-PEEM instruments today are located at undulator beamlines, Fig. 10.1, which use a series of magnetic poles that interact with the high energy electron beam of the accelerator as a source of very high brightness and intense x-rays. A special type of undulator, the elliptically polarizing undulator, or EPU, produces x-rays of variable polarization:

1. p-polarized, which is polarized within the plane of incidence and has an electric field vector component perpendicular to the surface
2. s-polarized, which is polarized parallel to the surface; or
3. circularly polarized.

Polarization control is particularly useful for the study of magnetism, bond orientation, and orbital structure.

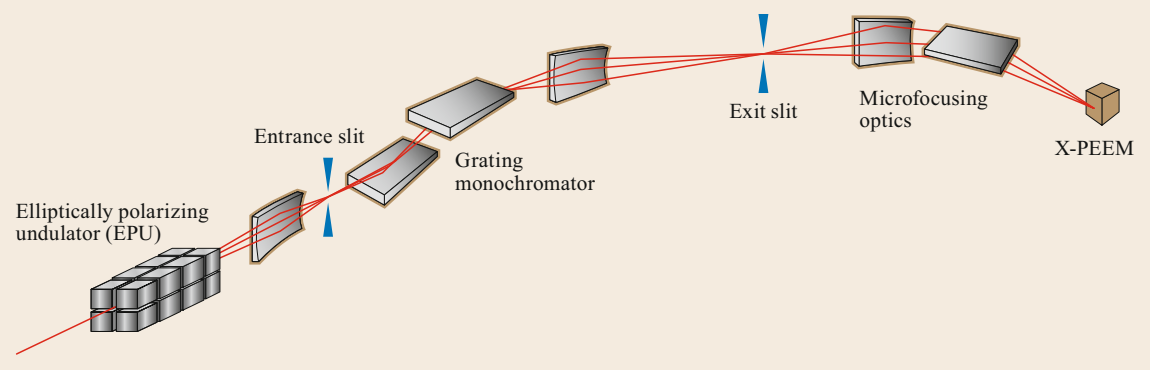

Fig. 10.1 Layout of the X-PEEM beamline 11.0.1.1 at the Advanced Light Source

The x-rays produced by the storage ring are transported through a beamline to the experiment. In a soft x-ray beamline, an optical grating monochromatizes the radiation with an energy resolution typically from a few tens to a few hundreds of millielectronvolts. X-ray photoemission electron microscopes are often used in an energy range above 100 and below 2000 eV, called the soft x-ray range, which spans x-ray absorption edges of many important elements, in particular of the light elements carbon, nitrogen, and oxygen; the transition metals vanadium over iron and cobalt to nickel; and the rare earth elements, which include the ferromagnets gadolinium and terbium. The x-rays are brought to the sample by mirror-based x-ray optics that match the x-ray spot size to the field of view of the microscope, which is usually between 1 and 100 µm. The electron optic system of the PEEM microscope then projects the x-ray-generated electron yield of the sample with high resolution and magnification onto a detector.

10.2.2 The X-Ray Absorption and Photoemission Process

When soft x-rays are absorbed by matter, electrons are excited from core levels into unoccupied states, leaving empty core states, Fig. 10.2. Additional secondary electrons are created by the decay of the core hole. This creates a cascade of excited electrons, some of which penetrate the sample surface and are then collected by the PEEM optics. A wide spectrum of electrons is emitted, with energies between the energy of the absorbed x-ray photon and the work function of the sample. This wide energy spread is one principal source of optical aberration, since electron lenses are chromatic, i. e., they focus at different spots depending on the energy and escape angle of the electron.

In the case of x-ray illumination, the distribution of the low-energy secondary electrons can be approximated by $n_e \sim E/(E+W)^4$, where W is the work function of the material and E is the kinetic energy of the electron [10.42]. In Fig. 10.3, modeled electron distributions in response to x-ray and UV illumination are compared. Note that for X-PEEM, electrons with a much wider range of energy contribute to the image. Therefore, X-PEEM instruments typically have lower spatial resolution than UV-PEEM instruments unless electron energy filters are employed. The effective mean free path λ_{el} of the low-energy secondary electrons that leave the sample sets a limit to the probing depth of the technique. In metals, a λ_{el} of 1.5–2 nm is typical [10.43]. In polymers, the effective mean free path is at least twice as large [10.44, 45]. Image contrast can still be obtained through coatings with a thickness of several times the effective mean free path, and nanometer-thick metal film

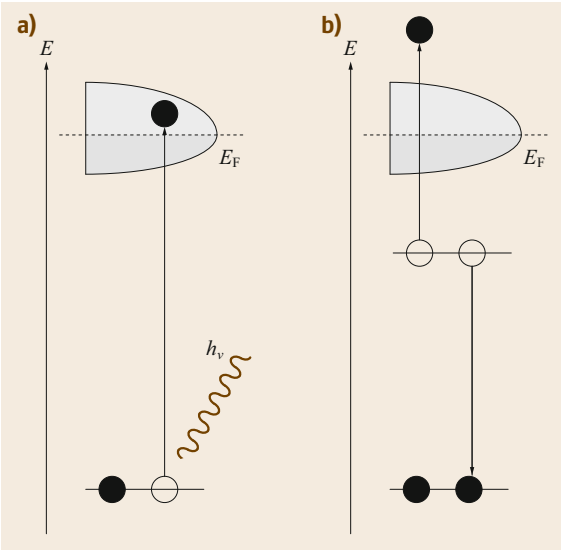

Fig. 10.2 **(a)** Excitation of a core electron into an empty valence state after x-ray absorption. **(b)** Auger decay of the core hole. A cascade of low-energy electrons is created, some of which escape into vacuum and are detected

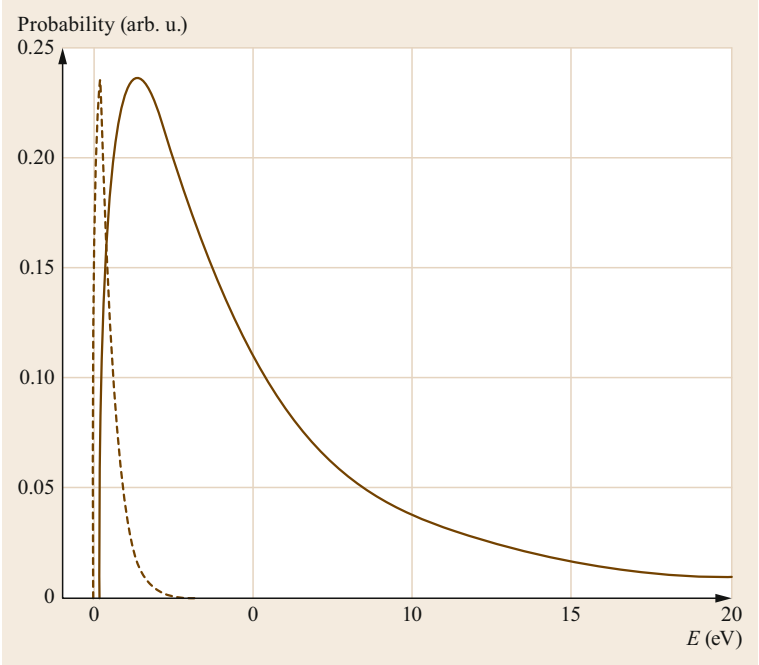

Fig. 10.3 Energy distribution of the emitted secondary electrons excited by x-rays (*solid line*) and UV light (*dashed line*)

coatings are often used to protect samples that are transported through air before imaging.

The energy-integrated electron emission of the sample is called the total electron yield (TEY) and is proportional to the x-ray absorption coefficient averaged over the probed thickness: the higher the x-ray absorption in this near surface region, the more photons are being absorbed there and the more electrons are being emitted from the sample. This rule holds as long as the electron escape depth is much shorter than the x-ray penetration length. Near absorption resonances, at which the x-ray absorption is very high, saturation effects need to be taken into account [10.46]. X-PEEM projects the lateral distribution of the electron emission and thereby maps the local x-ray absorption of the sample as a function of the x-ray energy. X-PEEM is a full-field imaging technique and a so-called spectromicroscopy technique; x-ray absorption spectroscopy (XAS) spectra from many sample locations can be recorded in parallel by acquiring electron emission images as a function of the x-ray energy.

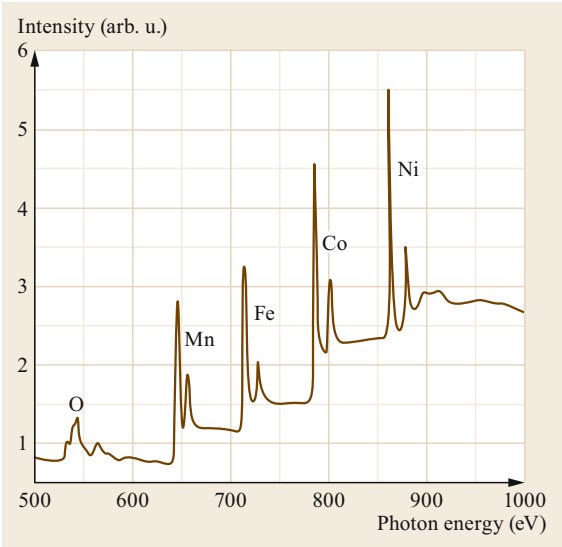

Fig. 10.4 X-ray absorption spectrum measured by recording the total electron yield of a multicomponent sample consisting of layers of Co and FeMn on a NiO(001) substrate

10.2.3 Image Contrast in X-PEEM

Contrast in X-PEEM arises from the element, chemistry, and magnetism-specific absorption and photoemission of materials, but artifacts originating from the topography of the sample surface also often appear; such topographic features shape the electrical potential close to the sample and modulate the image intensity near defects. If a contrast aperture is used, PEEM becomes very sensitive to the takeoff angle of the emitted electrons, and images will display surface-angle-dependent contrast. Usually, experimenters seek to minimize topographic contrast by preparing smooth samples, e. g., single crystals, polished surfaces, or films grown

on flat substrates, because sample roughness can limit the image resolution. Since topographical contrast appears for incident photons of any energy, dividing two images that were acquired at different energies is a common technique to remove artifacts. The sample is an integral part of PEEM electron optics, and the optimum resolution can only be achieved on optically flat surfaces. The effect of roughness and sample tilt are discussed in [10.47, 48].

Spectroscopic image contrast will be discussed in detail in Sect. 10.5; we will only give a short summary here. Elemental contrast is a consequence of the large enhancement of the absorption of x-rays when the energy of the x-rays is sufficient to excite a core level electron into an empty valence state. Resonant absorption of x-rays, promoting electrons from core states into narrow valence states near the Fermi level, further increases the absorption near the absorption edge and result in so-called *white lines*, characterized by a strongly enhanced emission of photoelectrons and secondary electrons (Fig. 10.4). When the photon energy is tuned to a specific absorption edge, areas that predominantly contain that particular element light up in the X-PEEM image.

The sharp variation in absorption and electron emission near an absorption edge is called the near edge x-ray absorption fine structure, or NEXAFS. NEXAFS is selective regarding the electronic state and chemical environment of the atom that absorbed the x-ray photon [10.49]. This chemical and electronic sensitivity is due to the fact that, close to the absorption edge, resonantly excited core electrons are lifted into and, therefore, probe valence states. For example, carbon NEXAFS spectra show features that can be associated with molecular orbitals, allowing a fingerprint analysis [10.49, 50]. In inorganic compounds, the NEXAFS spectrum is often used to determine oxidization states.

10.3 Uncorrected PEEM Microscopes

Most photoemission electron microscopes share some common characteristics. Modern microscopes use two, three, or more lenses, and usually at least an objective, an intermediate or transfer lens, and a projector lens. The electron optics of a typical non-aberration-corrected PEEM microscope are outlined in Fig. 10.5. Microscopes use electrostatic, magnetic, or compound magnetic-electrostatic lenses. The microscope that is described here is based on electrostatic lenses. The sample is located in front of an objective lens, which collects UV- or x-ray-generated electrons from within a wide solid angle. In a cathode lens microscope, the sample and objective lens form an immersion lens, and the sample is an integral part of the imaging system. A strong acceleration field of typically about 10 kV/mm accelerates the electrons between the sample, acting as the cathode, and the outer electrode of the objective lens, acting as the anode. The strong acceleration limits the relative energy spread and the angular spread of the electron beam entering the microscope and produces a collimated electron beam. The accelerating field, the objective lens, and the contrast aperture in the back focal plane of the objective or of a downstream transfer lens strongly determine the resolution and transmission of the system. In choosing different aperture sizes, spatial resolution can be traded for microscope transmission by limiting the angular acceptance of the microscope. A multipole stigmator-deflector is often located close to the back focal plane

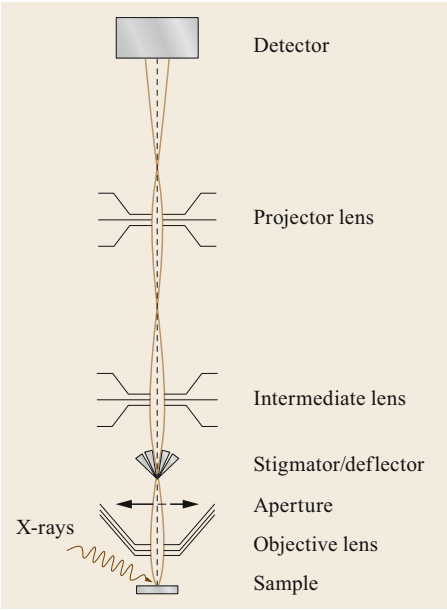

Fig. 10.5 Electron optical layout of a photoemission electron microscope. X-rays illuminate the sample, and the emitted electrons are accelerated by the strong electric field between the sample and the objective lens. The objective lens and the projector optics form a magnified image on an electron-sensitive detector. An aperture is used as a contrast filter and improves the spatial resolution. Deflector and stigmator plates correct some low-order aberrations ►

of the objective lens to compensate for astigmatism and alignment errors. The intermediate and projector lenses transfer and magnify the image onto a micro-channel plate or a phosphor screen. This phosphor transforms the electron into a visible light image, which is digitized by a CCD camera. The design of the sample stage in a PEEM microscope and its relative registration to the objective lens are critical. Any vibration or drift is magnified by the electron optics and reduces the microscope's spatial resolution. Significant mechanical misalignment of the sample or of the electron lenses causes astigmatism and higher-order aberrations and can result in resolution loss.

10.3.1 The Objective Lens

The objective lens is the most important component of the electron optical system. Triode and tetrode cathode lenses have been used. *Chmelik* et al. compared several types of cathode lenses [10.51]. *Rempfer* et al. analyzed different objective lens aberrations based on extensive electron optical bench measurements [10.13, 15].

The lens evaluation occurs in four steps:

1. Calculation of the field distribution of the lens
2. Calculation of the electron trajectories and the electron optical properties
3. Evaluation of the interaction of the lens with other parts of the electron optics, and
4. Tolerance analysis in regard to mechanical errors.

Often an analytical treatment is not possible, and numerical methods must be used. A charged particle optics (CPO) program was developed by *Harting* and *Read* for solving charged particle optics problems using the surface charge method [10.52]. Munro developed a series of electron optics programs using the finite element method, which was reviewed in [10.53, 54]. EOD is a program for the design of electron microscopes and was developed by *Zlamal* and *Lencova* [10.55]. SIMION 3D, developed by *Dahl* [10.56], is an electrostatic and magnetic field modeling program that solves the field using a finite element method and traces the motion of electrons using a fourth-order Range–Kutta integrator. Figure 10.6 shows the equipotential contours of a tetrode objective lens, calculated using SIMION. The acceleration field is approximately uniform in the vicinity of the optical axis, except close to the anode aperture. The aperture acts as a thin diverging lens [10.15, 57].

The objective lens can be characterized by the trajectory of the principal rays, the field ray, and the axial ray (Fig. 10.7). The calculation treats the electrodes as a single lens because the fields overlap, but it is instructive to describe the objective lens optic system as being composed of a) the accelerating field, b) a weak diverging lens, and c) a *unipotential* or *einzel* lens, a lens in which the image and object-side electrodes are on the same potential. The acceleration field forms a virtual image at unit magnification at twice the sample distance L. The weak diverging lens created by the aperture of the first electrode forms another virtual image at distance $L/3$ behind the sample. It is demagnified by $M = 2/3$. Finally, the unipotential lens forms a real image with a typical magnification of $M = 10–40$ [10.20, 23, 58].

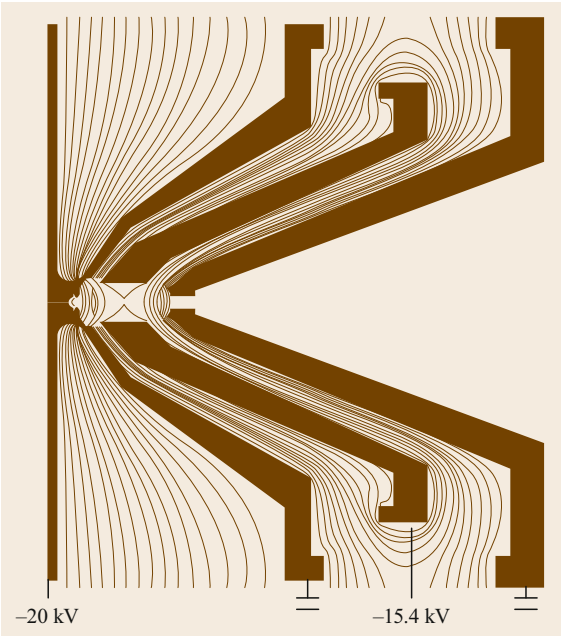

Fig. 10.6 Equipotential contours of the electric field of an electrostatic PEEM objective lens at 20 kV sample voltage

10.3.2 The Intermediate and Projector Lenses

The intermediate and projector lenses magnify the image of the objective lens without distortion to reach a final magnification typically between 30 and 4000. The angle and energy-dependent aberrations of the intermediate and projector lenses are negligible because the energy and angular spread of the electron beam are small here. However, the distortion aberrations need to be minimal because the object size after magnification by the objective lens is significant, fractions of a millimeter or more. Therefore, the intermediate and projector lenses are designed to work at minimum focal length. As the excitation of the electrostatic lens is increased, its focal length decreases, and the object-side focal point enters the lens field. The distortion coefficient can reach zero at minimum focal length. This type

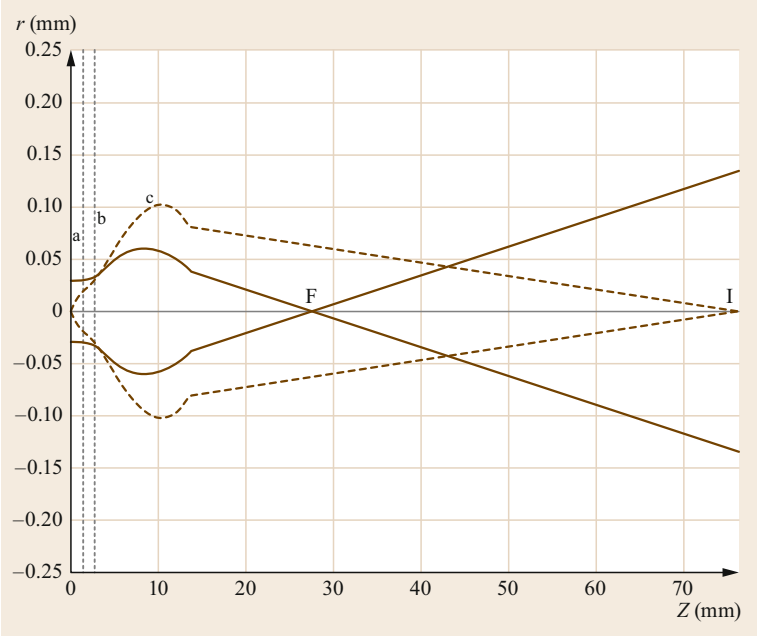

Fig. 10.7 Principal electron rays in three regions near the objective lens: region a, the accelerating field, region b, the weakly diverging field, and c, the unipotential lens. *Dashed line*: axial ray; *solid line*: field ray; F: back focal plane; I: image plane

of lens was examined in detail by *Lencova* [10.59] and *Rempfer* et al. [10.13, 14].

10.3.3 Transmission and Spatial Resolution of PEEM

The microscope transmission and spatial resolution determine the quality of a PEEM microscope. *Bauer* used these two quantities to define a quality factor [10.60]. The spatial resolution determines how well spatial details are preserved, and the transmission determines the noise level in an image and the acquisition speed [10.61, 62].

Transmission

The microscope transmission is defined as the fraction of emitted electrons that reach the detector. To reduce optical aberrations, most microscopes contain several apertures of different sizes that can be moved into the electron beam. Thus, transmission can be traded for resolution. The aperture confines the electron beam to the paraxial region and can also limit the energy acceptance of the microscope. Using $E/(E+W)^4$ for the electron energy distribution for a work function W and using Lambert's law for the electron angular distribution, the transmission of PEEM can be evaluated in a simple closed form

$$T = 1 - \frac{1}{\left[1 + \left(\frac{a}{f_i^*}\right)^2 \frac{U}{W}\right]^2} . \qquad (10.1)$$

Here, a is the aperture radius, U is the sample potential, and f_i^* is the image-side focal length of the objective lens. A high sample potential and a large aperture improve the transmission, whereas a long focal length and large work function reduce the transmission [10.63].

Figure 10.8 shows SIMION simulations of the angle and energy distribution of the electrons transmitted through apertures of different sizes. Every point represents one electron. Both the energy spread and the transmission decrease with decreasing aperture size. Note that high-energy, paraxial electrons still pass through the aperture. The resolution starts to be dominated by electron diffraction when the aperture size is lowered beyond a certain minimum value.

Spatial Resolution

The spatial resolution of microscopes is characterized by a spread function. The spread function describes the microscope image of a chromatic point source and a diverging electron beam. Diffraction, spherical, and chromatic aberrations are regarded as independent contributions and are added quadratically. The total resolution to a reasonable approximation is given by

$$r_{\mathrm{tot}} = \sqrt{r_{\mathrm{s}}^2 + r_{\mathrm{c}}^2 + r_{\mathrm{d}}^2} \qquad (10.2)$$

where the third-order spherical aberration is defined as

$$r_{\mathrm{s}} = C_{\mathrm{s}} \alpha^3 . \qquad (10.3)$$

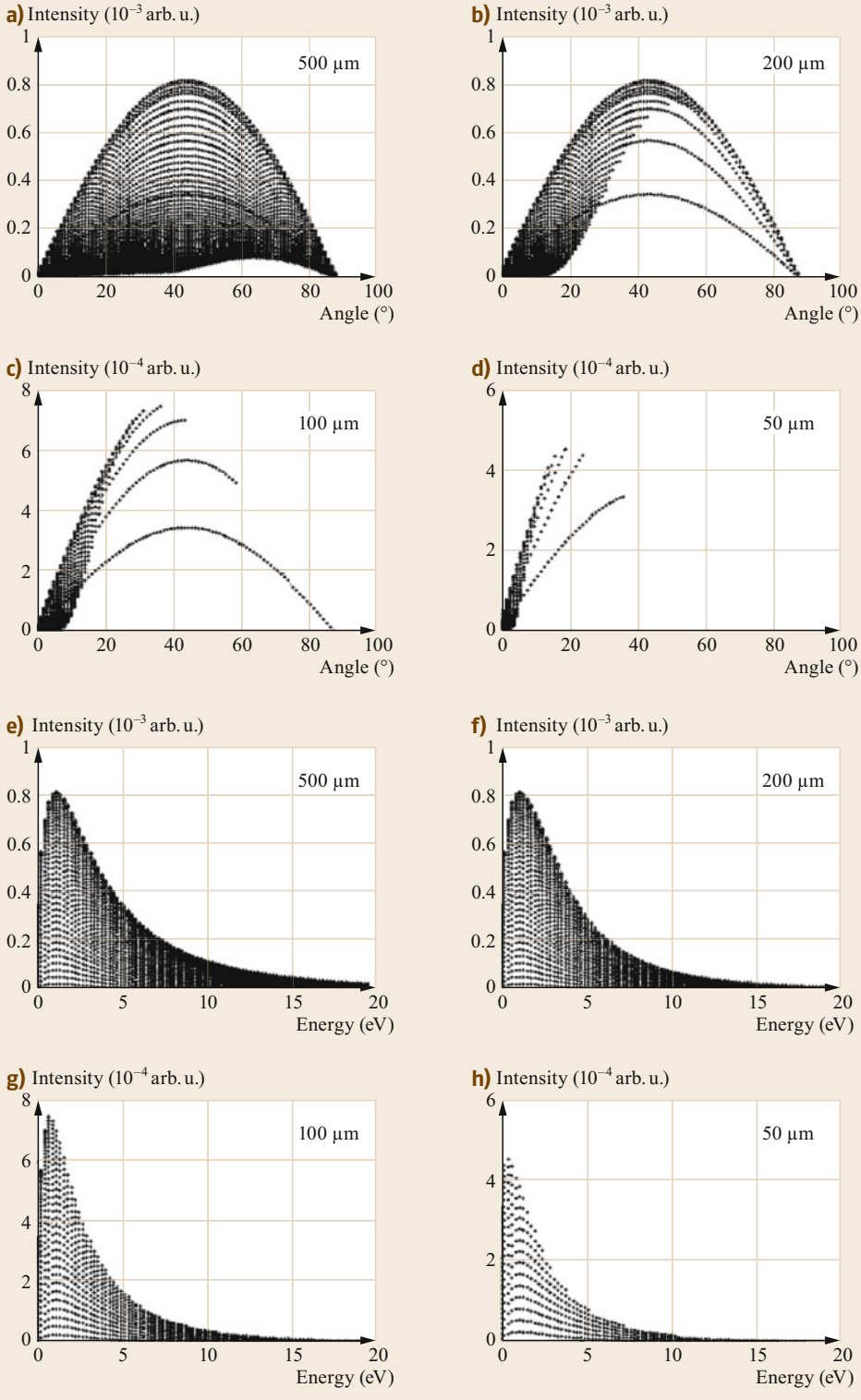

Fig. 10.8a–h SIMION simulations of the angle and energy distribution of the emitted electrons that are accepted by X-PEEM when apertures of different sizes are used. **(a–d)** show the angle and **(e–h)** the energy distribution

The first-order chromatic aberration is defined as

$$r_c = \frac{C_c \alpha \delta E}{E} , \tag{10.4}$$

and the diffraction disk is defined as

$$r_d = 0.61 \frac{\lambda}{\alpha} . \tag{10.5}$$

Here, C_s and C_c are the spherical and chromatic aberration coefficients, λ and E are the electron wavelength and the electron energy, δE is the electron energy spread, and α is the half angle of the pencil beam passing the back focal plane aperture. Though (10.2)–(10.5) can be easily solved, the results are often misleading because the contributions of aberrations and diffraction are not Gaussian and, therefore, only give a rough estimate of the microscope resolution.

An alternate way of characterizing the spatial resolution is by the spatial frequency transfer of the microscope. The intensity distribution of an image produced by a point object under incoherent illumination is called the impulse response function, $h(x, y)$. The object intensity distribution, $f(x, y)$, and the image intensity distribution, $g(x, y)$, are related by the convolution equation

$$g(x, y) = \iint f(x_1, y_1)\, h(x - x_1, y - y_1)\, \mathrm{d}x_1 \mathrm{d}y_1 . \tag{10.6}$$

After a Fourier transformation one obtains

$$G(f_x, f_y) = F(f_x, f_y) \cdot H(f_x, f_y) . \tag{10.7}$$

G, F, and H are Fourier transforms of $g(x, y)$, $f(x, y)$, and $h(x, y)$. The function $H(fx, fy)$ is the complex optical transfer function (OTF), with real and imaginary parts

$$\mathrm{OTF}(f) = |H(fx, fy)|\, \mathrm{e}^{\mathrm{i}\varphi(f)} . \tag{10.8}$$

The real part $|H(fx, fy)|$ is called the modulation transfer function, or MTF, and the function $\varphi(f)$ is called the phase transfer function. Experimentally, the MTF is measured as the contrast with which spatial frequencies of an object are transferred to an image. Higher frequencies correspond to smaller object features. Figure 10.9 shows the measured and calculated MTF of the PEEM-2 microscope at the Advanced Light Source (ALS), assuming an extraction field of 20 kV and a 12-μm aperture. The MTF starts with unity modulation transfer at low frequencies and gradually drops at higher spatial frequencies. A transfer of one indicates that the spatial detail of an object at that frequency is perfectly transferred, while zero transfer indicates a complete loss of information. Values between 0 and 1 indicate partial transfer of spatial frequencies and a reduced contrast. The Rayleigh criterion for spatial resolution is equivalent to a 9% contrast transfer, which is reached for a frequency corresponding to a feature size of 35 nm for this microscope. Often, a higher contrast is required in experiments. At about 80 nm, PEEM-2 reaches 40% contrast transfer.

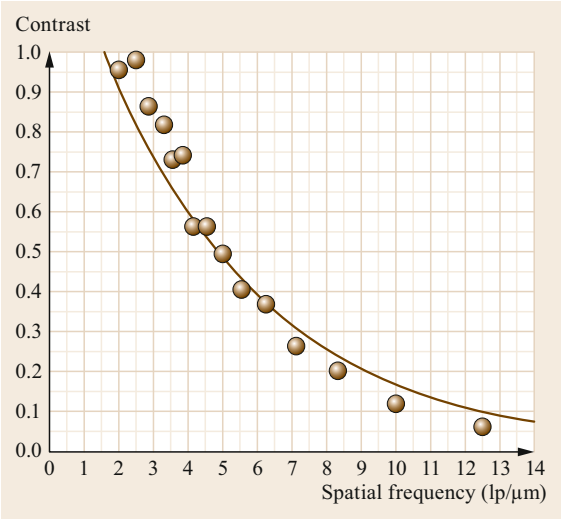

Fig. 10.9 Measured (*dots*) and calculated (*solid line*) modulation transfer function (MTF) of PEEM-2 at the ALS

10.4 Aberration-Corrected PEEM Microscopes

The improvement in resolution of light and electron microscopes over the last two centuries is compared in Fig. 10.10 [10.64]. At the beginning of the twentieth century, the light microscope had reached its best resolution after the invention of aberration correction by E. Abbe, using a combination of a concave and a convex lens, called an achromatic lens. The resolution of the electron microscope soon surpassed that of optical microscopes because of the much shorter wavelength of kilovolt electrons—effectively removing the effect of diffraction, if electrons of sufficiently high energy are used. The resolution of uncorrected electron microscopes is mainly limited by lens aberrations. Among these aberrations, astigmatism, coma, and field distor-

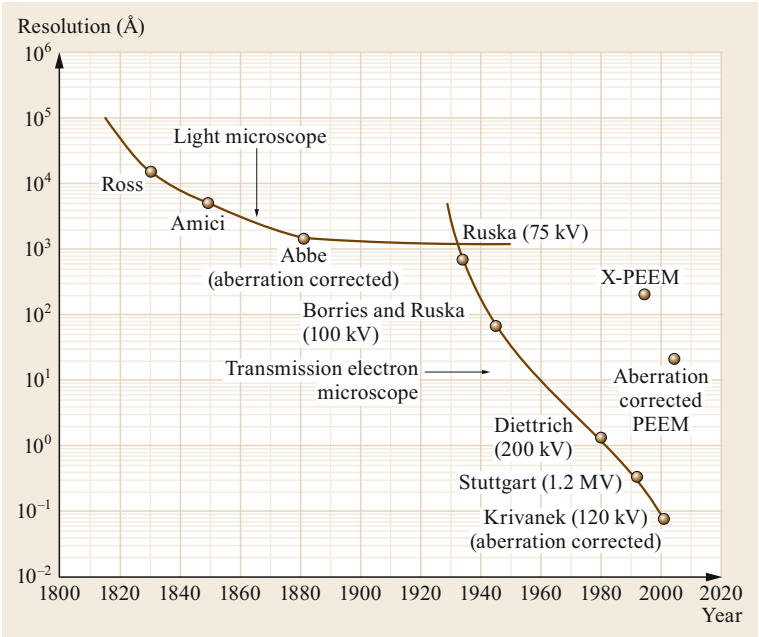

Fig. 10.10 History of microscopy techniques and evolution of spatial resolution. Shown are significant steps in the development of optical microscopy, electron microscopy, and X-PEEM. (After [10.64])

tions can be easily corrected or, close to the optical axis of the microscope, they can be disregarded because they are small. Early in the development of electron optics theory, *Scherzer* showed that simple electron lenses always suffer from two other important image errors: chromatic and spherical aberrations [10.65]. The electron optical analogue to a light optical achromatic lens does not exist. Different approaches have been tried to remove these aberrations by relinquishing one of the conditions of Scherzer's theorem, which only applies to simple lenses [10.66]. Multipole aberration correctors, which use a field that is not rotationally symmetric, have been successfully used in low-voltage scanning electron microscopy (SEM) [10.67], in transmission electron microscopy (TEM) [10.68, 69], and in scanning transmission electron microscopy (STEM) [10.70, 71]. X-PEEM instruments have much larger aberration coefficients than SEM or TEM instruments, because of the large energy width of the secondary electron distribution, the low initial electron energy, and the large field of view. Therefore, the aberrations of X-PEEM microscopes have to be corrected using an electron mirror, which is designed to have opposite chromatic and spherical aberrations compared to the objective lens. In the following, we will focus on the optical design of the ALS PEEM-3 microscope, which was optimized for the wide energy spread of the electrons imaged by a non-energy-filtered X-PEEM.

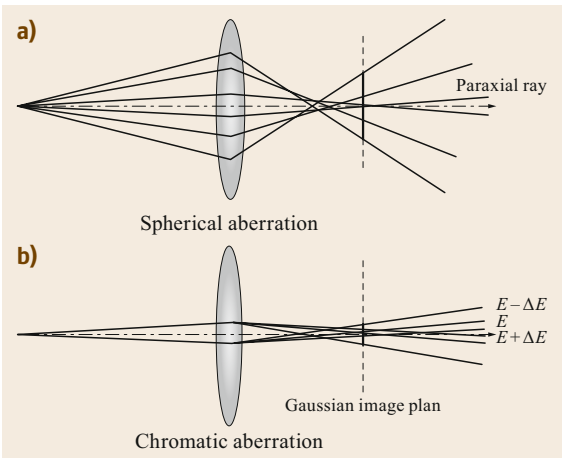

Fig. 10.11a,b Illustration of (a) spherical and (b) chromatic aberrations of an electron lens. Off-axis electrons and electrons with different energy are focused at a different position

10.4.1 Aberrations of an Electron Lens

The electron trajectories in an electron lens are affected by spherical and chromatic aberrations, Fig. 10.11. A detailed review of electron optical aberrations can be found in the chapter by Krivanek and Hawkes. We concentrate here on the two dominant low-order aberrations for X-PEEM, the third-order (in angle) spherical aberration and the first-order (in angle), first-rank (in energy) chromatic aberration. The Gaussian image plan is defined as the intersection of the paraxial ray with the optic axis. The spherical aberration refers to the variation of the focal distance with the angle of a ray from the paraxial ray. An electron passing the lens far

from its center experiences a higher field and is focused more strongly. The focus lies in front of the image plane. The chromatic aberration refers to the variation of the focal distance with the electron energy. Slower electrons experience the field for a longer time and are focused more strongly. The focus lies in front of (slow electrons) or behind (fast electrons) the image plane.

Figure 10.12 shows the resolution of a typical X-PEEM with a 2-mm acceleration gap and 20-kV acceleration field for a 4-eV work function, broken down according to the source of the aberration. Dominant are the aberration by the accelerating field and the chromatic aberration of the lens. Although the resolution can be improved by using a very small aperture, the usefulness of this approach is limited because of the severe reduction in microscope transmission and the onset of diffraction at very small aperture sizes. An ultimate resolution of close to 20 nm has been achieved in several instruments [10.20, 72–74]. Aberration correction significantly improves the ultimate resolution beyond this limit and can also increase the transmission and electron optical efficiency of X-PEEM at moderate resolution by a factor of up to 100 [10.75].

10.4.2 An Aberration-Corrected Microscope Using an Electron Mirror

The idea of using an electron mirror to correct the chromatic and spherical aberration of a round lens dates back more than half a century [10.76, 77]. Extensive studies of electron mirrors have been performed by *Kel'man* et al. [10.78, 79], *Dodin* and *Nesvizhskii* [10.80], *Rempfer* et al. [10.81–83], *Shao* and *Wu* [10.84, 85], and *Rose* and *Preikszas* [10.86, 87]. An electron mirror uses a reflecting electrode with a sufficiently high negative potential to reverse the propagation direction of the electron beam. In 1990, *Shao* and *Wu* proposed using an electron mirror with more than two electrodes to be able to freely adjust the aberration coefficients [10.84]. Through numerical analysis of a four-electrode electric mirror, *Shao* and *Wu* showed that spherical and chromatic aberrations can be adjusted electrically without changing the image distance of the mirror. Later, a more sophisticated theoretical model using a time-dependent perturbation method was developed by *Rose* and *Preikszas* [10.86, 87]. Integral expressions for the aberration coefficients of an electron mirror were derived, and higher-order aberrations were studied. A prototype of an aberration-corrected x-ray microscope is the PEEM-3 microscope at the ALS [10.40]. The microscopes relies on the correction of chromatic and spherical aberrations using a hyperbolic electron mirror, which was suggested by *Rempfer* et al. [10.83].

Figure 10.13 shows a schematic overview of the electron optics of PEEM-3. The electrons travel through the microscope along the dashed lines. The objective lens, together with the field lens, forms a telescopic round lens system. This allows the mirror to run in so-called symmetric mode, in which first-order chromatic distortion and third-order coma vanish, and curvature-of-field effects are reduced [10.88]. An electrostatic

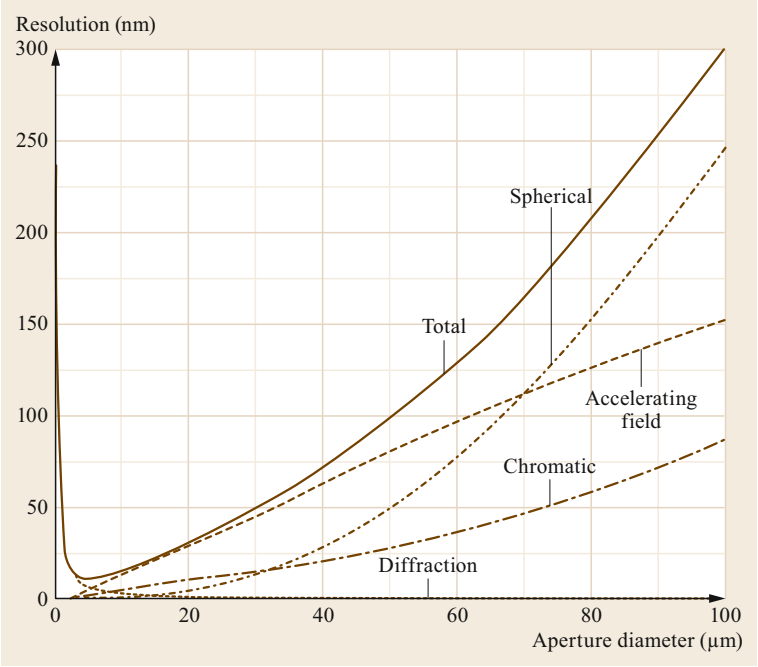

Fig. 10.12 Contributions of various aberrations (aberration of the accelerating field, chromatic aberration of the objective lens, spherical aberration of the objective lens, contribution of diffraction) to the total resolution limit of uncorrected PEEM. The sample voltage is 20 kV, the gap = 2 mm, the work function $W = 4$ eV

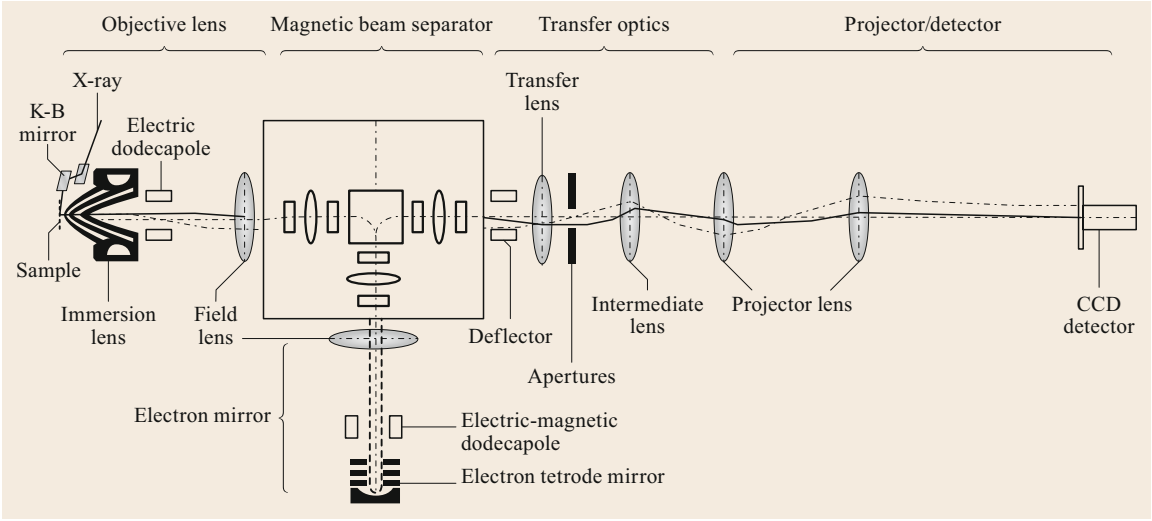

Fig. 10.13 Layout of the aberration-corrected PEEM-3 at the ALS. An electron mirror is used as the aberration corrector

dodecapole deflector steers the beam into the magnetic separator and corrects astigmatism. For a single deflection of 90°, the beam separator images its entrance plane 1 : 1 onto its exit plane, without introducing aberrations of second order. The electron mirror images the mirror-side exit plane of the beam separator back onto itself. In order to cancel coma generated by the mirror, the magnification of the mirror is chosen to be −1 [10.89]. The separator then transfers the aberration-corrected image to the projector optics, which magnify the image.

The PEEM-3 electron mirror has four rotationally symmetric electrodes, and the reflecting electrode is a segment of a sphere with a radius of 5.6 mm. The inner electrode is held at ground voltage, while the potentials of the other electrodes provide three free knobs to set the focal length, the chromatic aberration correction, and the spherical aberration correction of the mirror. Figure 10.14 shows the equipotential distribution and correction region of the mirror. This region is sufficiently large to correct the microscope aberrations in various modes of operation.

10.4.3 The Beam Separator

The task of the magnetic beam separator is to separate the aberration-corrected beam leaving the mirror from the beam that enters the mirror. A separator with very small aberrations is critical for the performance of an aberration-corrected PEEM microscope.

Figure 10.15 shows the 90° beam separator that is in use in the ALS PEEM-3. The separator consists of three round lenses, one dipole magnet, and six electrostatic quadrupoles. Round lenses are chosen to be the main focusing optics. Weak electrostatic quadrupoles are used to form a stigmatic image after each 90° bend. Each 90° bend is mirror symmetric about the center and acts as a telescope in the x–z and the y–z plane. The linear dispersion and the second-order axial aberrations, which are not corrected within each 90° bend, cancel to zero after the second pass through the separator, because of the negative unity magnification of the mirror. Calculations were performed to predict the chromatic and spherical aberrations of PEEM-3 [10.90]. The PEEM-3 beam separator uses electrostatic lenses instead of fringe fields for image focusing and is robust regarding the details of the magnetic field in the separator. A simple dipole magnet can be used, and the demands for power supply stability and mechanical tolerances are relatively low.

10.4.4 Resolution and Transmission Modeling of an Aberration-Corrected PEEM

Aberration correction significantly improves both the spatial resolution and the transmission. An ensemble of electrons with different initial energy and emission angle were sent through a model of the electron optics, with intensity weighted with the probability of each emission energy and angle. The diffraction effect was calculated for each electron in the ensemble, and the result was summed up to yield the point spread function. The resolution was defined as the distance between the 15th and the 85th percentiles of the point spread function. The calculated resolution and transmission of ALS PEEM-3 are shown in Fig. 10.16, in comparison with the uncorrected ALS PEEM-2 [10.91]. PEEM-3

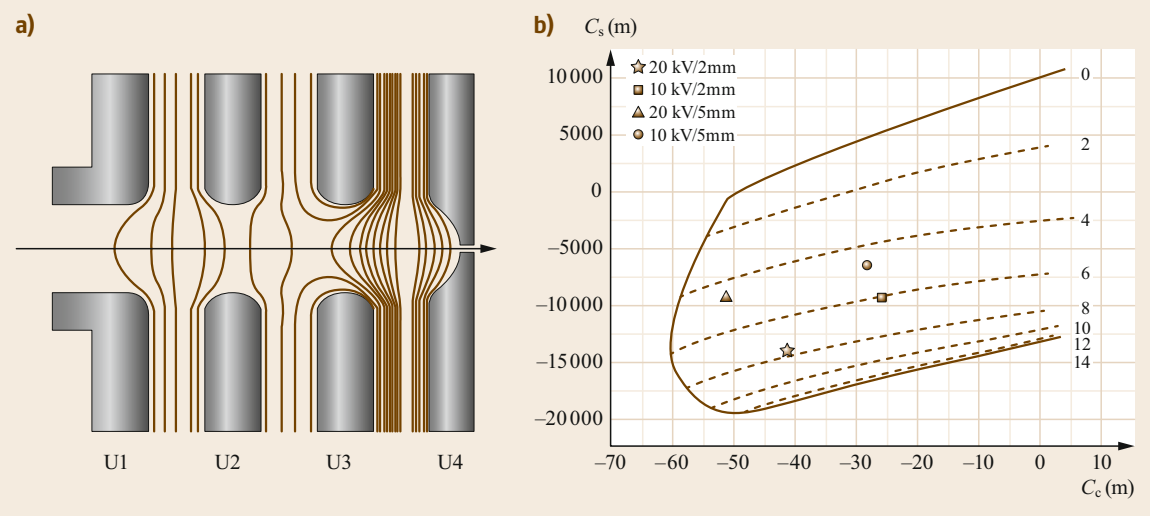

Fig. 10.14a,b Aberration correction by a tetrode electron mirror. **(a)** Equipotential contours. **(b)** The aberration region that can be corrected by the mirror

is designed to have two main operation modes, a high-resolution mode and a high-flux mode. Operating at 20 kV and a 2-mm working distance, the resolution for 100% transmission (no aperture used) is designed to reach a resolution of 50 nm using the mirror corrector, a significant improvement over PEEM-2, which reaches only 440 nm. Using a small aperture, the optimum resolution is predicted to reach 5 nm at 2% transmission, as opposed to 20 nm at 1% transmission for PEEM-2.

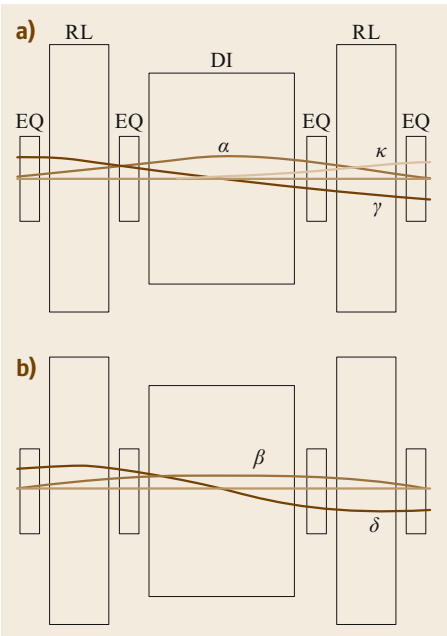

Fig. 10.15a,b Layout and principal rays in the **(a)** x–z and **(b)** y–z plane of one 90° sector of the PEEM-3 separator. Two 90° bends transport the beam into the mirror and back to the projector optics. One dipole (DI), two round lenses (RL), and four quadrupoles (EQ) are used

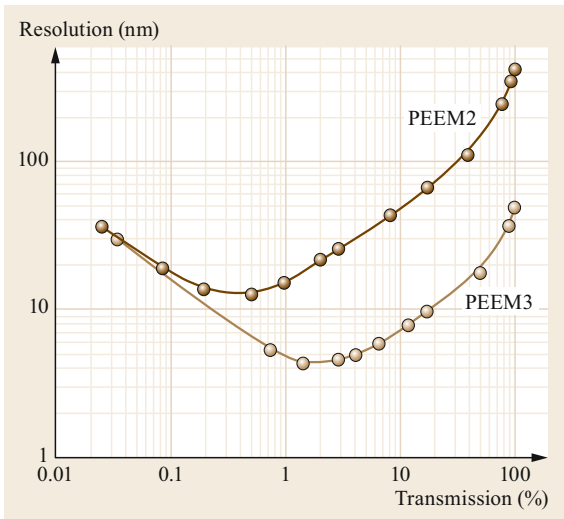

Fig. 10.16 Comparison of calculated resolution versus transmission of the ALS PEEM-2 (*light brown symbols*) and PEEM-3 (*dark brown symbols*). The acceleration potential is 20 kV, and the sample–lens distance is 2 mm

10.5 Spectromicroscopy: Electronic Structure, Chemistry, and Magnetism

The spectroscopic acquisition of microscopic data is called *spectromicroscopy*. X-PEEM microscopes at x-ray sources are used to record data, for example:

1. As a function of the energy of the photon beam: x-ray absorption spectroscopy (XAS)
2. As a function of the pass energy of the photoelectrons transmitted through a microscope equipped with an energy analyzer: x-ray photoelectron spectroscopy (XPS) and angle-resolved photoemission spectroscopy (ARPES)
3. As a function of the x-ray polarization: x-ray dichroism spectroscopy.

10.5.1 Imaging of Ferromagnetic and Antiferromagnetic Domains Using X-Ray Circular and Linear Dichroism

Figure 10.17 shows XAS spectra near the Co and Fe L-edge, measured on a $Co/LaFeO_3$ double layer that was grown on a $SrTiO_3$ substrate. Note that the post-edge intensity is higher than the pre-edge intensity since photons now have sufficient energy to promote L-edge core electrons into empty states via a dipolar transition. Dipole selection rules require that the transition is from a 2p state into a d or s-symmetry valence state. The spin–orbit interaction splits the transition, resulting in the L_3 branch from the $2p_{3/2}$ core state having lower energy and the L_2 branch from the $2p_{1/2}$ core state having higher energy. The sharp resonances visible in these spectra are due to resonant excitation of electrons into the relatively narrow, empty d-states near the Fermi level. The recorded spectra of these magnetic materials also show magnetic dichroism, a change of the x-ray absorption depending on the polarization or magnetic state of the sample.

X-ray magnetic circular dichroism (XMCD) is a widely used method to study magnetic thin films and surfaces [10.93]. The wide availability of polarized and tunable x-rays from synchrotron sources has played an important role in the success of x-ray dichroism techniques. The last 30 years have seen much progress following the first XMCD spectroscopy measurements at the important transition metal L-edges in 1987 by *Schütz* et al. [10.94], the first x-ray imaging of ferro-

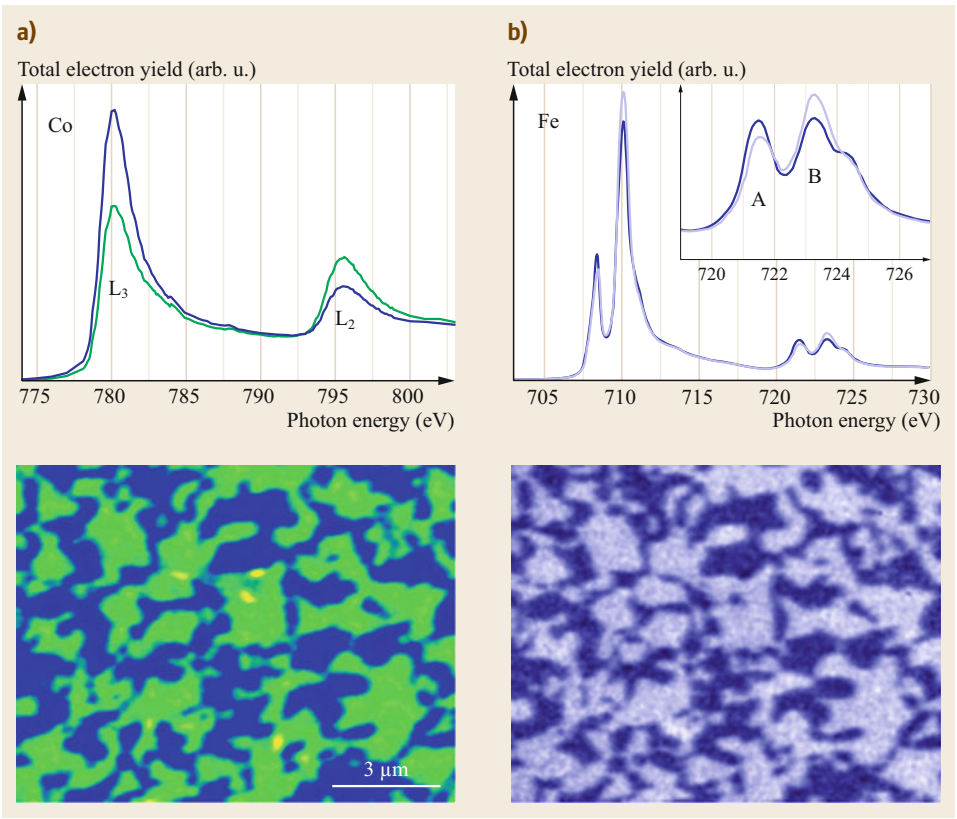

Fig. 10.17a,b Co spectra and images **(a)** and Fe spectra and images **(b)** of a double layer of $Co/LaFeO_3$, grown on $SrTiO_3(001)$, which were acquired using polarized x-rays. The XMCD and XMLD images show the layers' ferromagnetic and antiferromagnetic structures. (From [10.92])

magnetic (FM) domains in 1993 by *Stöhr* et al. [10.19], and the first x-ray imaging of antiferromagnetic (AFM) domains by *Stöhr* et al. and *Scholl* et al. [10.95, 96] in 2000, followed by demonstrations of picosecond time-resolved stroboscopic imaging by *Vogel* et al. and *Choe* et al. in 2004 [10.97, 98]. Circularly polarized x-rays measure the direction of the atomic magnetic moment of a ferromagnet relative to the polarization vector of the x-rays. The two NEXAFS spectra in Fig. 10.17 were acquired using circularly polarized x-rays from regions of the sample with a direction of the magnetization parallel (*blue*) and antiparallel (*green*) to the x-ray polarization direction. In the presence of the spin–orbit interaction, electrons of one spin direction are predominantly excited by circularly polarized x-rays, which then sense the spin-dependent density of valence states. An imbalance of the occupation of the valence majority and minority spin states is characteristic for a ferromagnet and results in a magnetic circular dichroism, a polarization and magnetization-dependent absorption of x-rays. So-called *sum rules* were developed to quantitatively determine the spin and orbital magnetic moment per atom from polarization-dependent NEXAFS spectra [10.99–101]. The angle and magnetization dependence of x-ray magnetic circular dichroism in the total absorption signal follows $I_{\mathrm{XMCD}} \approx \cos\alpha |M|$. It is linear in the magnetic moment M and follows a cosine dependence with the angle α, the angle between the x-ray polarization vector (parallel to the x-ray propagation direction) and the magnetization vector.

Linearly polarized x-rays probe the anisotropy of the electronic and magnetic structure and the occupation of orbital states and are particularly useful for the study of antiferromagnets. The NEXAFS spectra of the G type collinear antiferromagnet $LaFeO_3$ in Fig. 10.17 show a characteristic change in the near edge structure depending on the direction of the antiferromagnet's magnetic axis relative to the linear x-ray polarization direction [10.46, 102–104]. In transition metal oxides, such as NiO, CoO, Fe_2O_3, Fe_3O_4, and $LaFeO_3$, an x-ray magnetic linear dichroism (XMLD) of up to $\approx 10\%$ has been observed. Linearly polarized x-rays probe the angle α between the x-ray polarization vector and the orientation of the magnetization axis of a collinear antiferromagnet. The magnetization dependence of the XMLD intensity is approximately given by $I_{\mathrm{XMLD}} \approx |M^2|$; $M^2|$ is the statistical average of the moment squared.

The large magnetization dependence of the x-ray absorption near a resonance has been successfully used for magnetic imaging, as reviewed by *Schneider* and *Schönhense* [10.23]. Such imaging is often done by acquiring two images at two different photon energies, e. g., the L_3 and L_2-edges of Co or the A and B-labeled resonances of Fe (Fig. 10.17 [10.92]). Alternatively, images acquired using different x-ray polarization states can be used: right and left circular for XMCD imaging and s-polarized (in the plane of the sample) and p-polarized (in the plane of incidence) for XMLD imaging. The images are either divided or subtracted to create a contrast image; frequently, the difference divided by the sum, the asymmetry, is also used. The contrast of this differential image encodes the local direction and magnitude of the magnetic moment and creates a domain map. Figure 10.17 shows such domain maps of the $Co/LaFeO_3$ double layer. These images illustrate the ability of X-PEEM to isolate the signal from individual layers by exploiting the element selectivity of XAS. Tuning the photon energy to the Co edge emphasizes the Co FM domain structure, while tuning the energy to the Fe edge shows the $LaFeO_3$ AFM domain structure. This element specificity of x-ray absorption is often used by researchers to study magnetic coupling effects. The surface sensitivity of X-PEEM leads to an enhanced sensitivity to the surface or shallow interfaces, which has been exploited in experiments on exchange bias systems and the interface magnetic structure between coupled ferromagnets and antiferromagnets [10.105, 106].

10.5.2 Magnetic Microscopy of Nanostructures

The direction of the magnetic moments in ferromagnets and antiferromagnets is determined by the magnetic anisotropy, which has local and intrinsic contributions, for example, the contribution of the crystalline anisotropy, which favors a magnetization along certain crystal axes; the contribution of the interface, which causes exchange bias; and contributions of long-range dipolar forces, which favor flux closure domain patterns. In exchange-coupled and laterally confined structures, the anisotropy can be tailored to create desirable magnetic properties, which then result in the complex domain images of Fig. 10.18. Nanowires of exchange-coupled $LaFeO_3/La_{0.7}Sr_{0.3}MnO_3$ (LFO/LSMO) films were imaged using XMCD and XMLD contrast at a temperature below the magnetic ordering temperature of both materials [10.107].

The crystal anisotropy and dipolar coupling force the magnetization of the ferromagnet LSMO along the zigzag nanowire. A spin–flop-type, perpendicular interface coupling between the ferromagnet and the antiferromagnet dominates in the wider wires and forces the magnetic axis of the antiferromagnet LFO perpendicular to the edges of the wire. As the wire narrows, an unforeseen anisotropy of the wire edges begins to

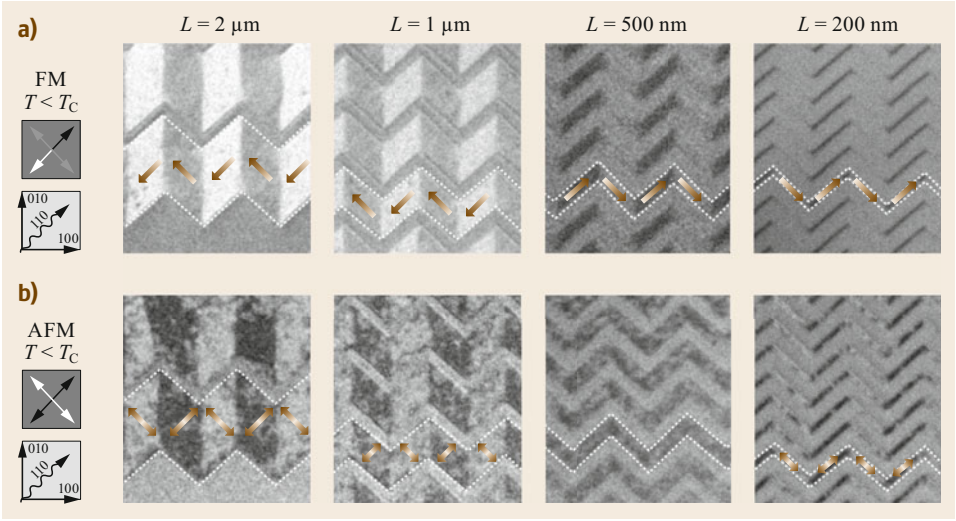

Fig. 10.18a,b X-PEEM images of ion-implantation-patterned LFO/LSMO thin film structures. The edges of the wires are parallel to the ⟨110⟩ direction, the easy magnetization direction of LSMO. The micrographs show the FM domain pattern in LSMO at $T = 100$ K **(a)**, and the corresponding (AFM) domain pattern in LFO **(b)**, for different pattern widths L. The experimental geometry and resulting X-PEEM contrast are illustrated in the schematics on the *left*. (Reprinted with permission from [10.107], copyright 2012 by the American Chemical Society)

dominate and turns the magnetic axis of antiferromagnet LFO parallel to the edges of the wire. This creates a frustrated system since edge anisotropy and interface anisotropy compete. Exploiting element specificity, X-PEEM imaging revealed the complex interplay of anisotropies in such nanostructured and coupled magnetic structures [10.108, 109].

X-PEEM, as a full-field imaging technique, is well suited for rapid time-lapse imaging experiments, e. g., of magnetization relaxation and of thermal fluctuations in dipolar-coupled nanomagnet arrays. Such nanomagnet arrays are studied to understand the process of magnetization relaxation and magnetically frustrated systems are often called artificial spin ice after the natural pyrochlore spin ice system. Figure 10.19 shows the thermal relaxation of an initially magnetically saturated $Ni_{0.8}Fe_{0.2}$ nanomagnet pattern towards its AFM ground state. The images were captured using XMCD contrast at the Swiss Light Source X-PEEM endstation [10.110]. The rate of fluctuations in a thermally active artificial spin ice system scales steeply with temperature, and high-speed magnetic imaging with nanometer resolu-

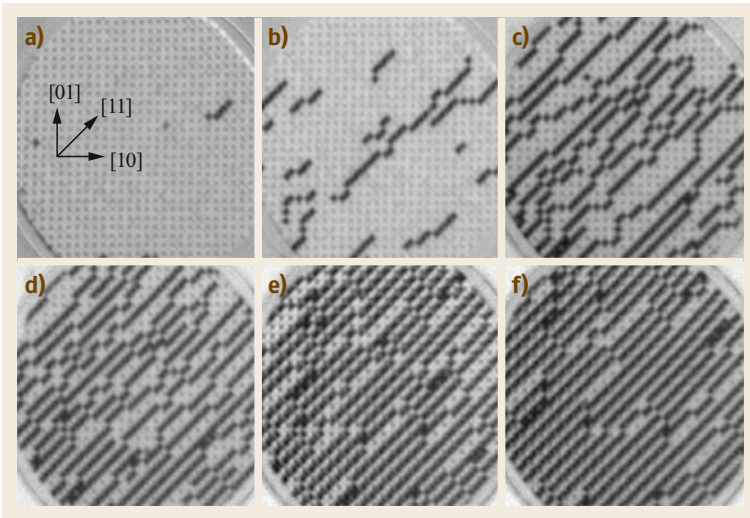

Fig. 10.19a–f XMCD images of the thermal relaxation process of *square ice*, artificial spin ice, from a saturated state towards its ground state **(a–f)**. The field of view is 20 µm. (Reprinted with permission from [10.110], copyright 2013 by the American Physical Society)

tion is needed for thermally active systems. Magnetic studies with a time resolution of seconds have been reported, mostly limited by the time needed to switch the x-ray polarization between exposures [10.111], but differential detection schemes using high frame rate detectors should allow magnetic time-lapse imaging at a higher frame rate, limited only by the available x-ray flux.

Magnetism studies often use a magnetic field to initialize a particular magnetic state. As a low-energy electron imaging method, X-PEEM is quite sensitive to magnetic fields. Typically, magnetic imaging experiments are conducted in remanence, following a magnetic field pulse, but miniaturized electromagnets have been developed that reduce the effect of the magnetic stray field by using a yoke with a very small gap. The remaining image distortions can be compensated by deflectors of the microscope. *Kronast* et al. conducted magnetic hysteresis measurements in fields of up to 20 mT while retaining high spatial resolution [10.112]. Their measurement of the magnetic properties of 18-nm-sized Fe nanocubes is shown in Fig. 10.20. A magnetic hysteresis loop was recorded by acquiring XMCD–PEEM images at the Fe edge while ramping up the magnetic field and then computing the field-dependent XMCD contrast of a single particle. The study demonstrates that the sensitivity of X-PEEM to magnetic fields can be overcome by careful engineering of the sample holder and by using appropriate corrector elements in the electron optics.

10.5.3 Spectromicroscopy Using NEXAFS, XPS, and ARPES

Besides its use in studying magnetism, X-PEEM has found other uses as a tool to characterize the chemical, orbital, electronic, and physical structure of surfaces and thin films. The light elements carbon, nitrogen, and oxygen are key chemical elements in polymers and biomaterials, and their K-edges lie in the soft x-ray range, to which many synchrotron-based X-PEEM microscopes have access.

As an example of high-resolution chemical mapping, we show a prototypical experiment on bioblends of polymers, which are of interest as composite materials with tunable properties. The biocompatibility of such bioblends was studied by X-PEEM at the carbon and nitrogen edges. NEXAFS spectromicroscopy was performed on thin films interacting with solutions of human serum albumin (HSA), an important blood protein. Figure 10.21 displays X-PEEM images of a polystyrene (PS)-polyactide (PLA) composite thin film brought into contact with HSA and imaged at two energies that are specific for PS (the π^*C=C resonance at 285.2 eV) and PLA (the π^*C=O resonance at 288.5 eV) [10.113]. NEXAFS reference spectra (*dark brown* and *medium brown*) of PS and PLA are shown as well. Both film components and the HSA (*light brown*) have characteristic spectra that, together with additional N-edge data, were used to differentiate between the three components at the surface of the sample and to create spatially resolved component maps. This was achieved by the method of singular value decomposition, which is essentially a least squares fit of reference spectra of the sample components to experimental X-PEEM spectra, pixel by pixel. This method has found wide application in the analysis of composite x-ray absorption spectra obtained using x-ray spectromicroscopy techniques, such as X-PEEM and scanning transmission x-ray microscopy (STXM) [10.114]. STXM and X-PEEM are complimentary techniques. In contrast to X-PEEM, STXM probes thicker films in transmission. In the cited study, the authors observed that blood protein covered both PS and PLA regions, leading to the purple and turquoise coloring of the color-coded maps in Fig. 10.21, but annealing led to a concentration of HSA along the lateral interfaces between PS and PLA regions [10.113].

A new spectromicroscopic technique for the structural and chemical characterization of biominerals that relies on x-ray-energy and polarization-dependent x-

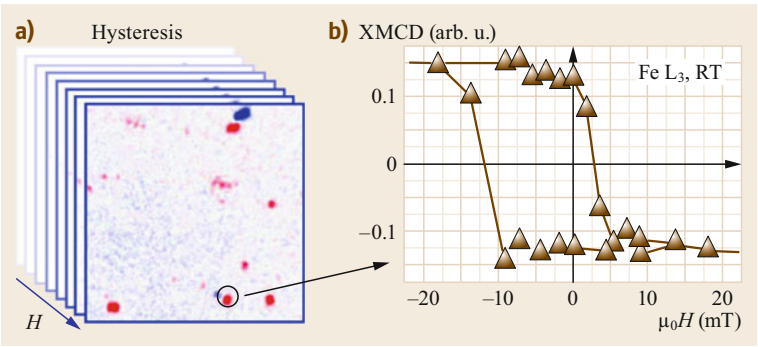

Fig. 10.20a,b Local hysteresis loops of 18-nm-sized Fe nanocubes measured in a magnetic field using XMCD–PEEM imaging. **(a)** *Blue* and *red* color indicate opposite magnetization directions in the XMCD image on the *left*. **(b)** A loop is computed by plotting the XMCD intensity of a particle as a function of the applied field. (Reprinted with permission from [10.112], copyright 2011 by the American Chemical Society)

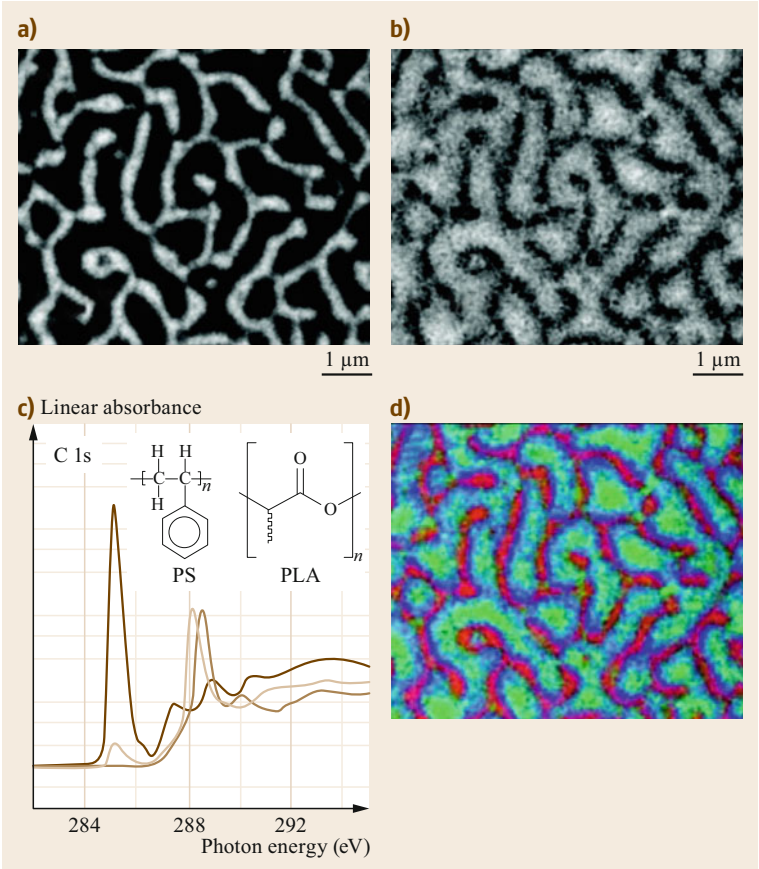

Fig. 10.21a–d NEXAFS component maps of human serum albumin (HSA) adsorbed on polystyrene (PS)-polyactide (PLA) thin films. **(a)** PS map, **(b)** PLA map, **(c)** carbon K-edge reference spectra of PS, PLA, and HSA, **(d)** the color-coded composite map, computed from C-edge and N-edge (not shown) data, shows the distribution of PS (*red*), PLA (*green*), and HSA (*blue*). (Reprinted with permission from [10.113], copyright 2009 by the American Chemical Society)

ray linear dichroism (XLD) contrast was developed by *Metzler* and *Gilbert* et al. in 2007; this technique is also called polarization-dependent imaging contrast (PIC) mapping [10.115]. PIC mapping is based on the so-called searchlight effect of x-ray linear dichroism: dipole transitions restrict electron excitation into orbitals that are aligned with the electric field or polarization vector of the x-rays, an effect that can be used to probe crystallographic orientation. For example, the x-ray absorption of orthorhombic aragonite depends strongly on the direction of the electric field vector of the x-rays relative to the *c*-axis of the crystal. By acquiring sequences of images at different directions of x-ray polarization, the local crystal orientation can be mapped [10.116]. Figure 10.22 shows PIC maps of two biominerals that were imaged using linear polarized x-rays [10.117]. Sample A shows the prismatic layer of the calcite shell of *Mytilus californianus*, a mussel native to the west coast of North America. Sample B shows a tunic spicule from the tunicate *Herdmania momus,* a sea squirt made of vaterite. Vaterite is the least stable polymorph of calcium and is quite rare. The intensity and angular phase of the XLD effect are displayed in color-coded PIC maps that are measured by rotating the x-ray polarization of the beam between p-polarization, which has a large component perpendicular to the surface of the sample, and s-polarization, which has a polarization vector parallel to the sample surface. The color encodes the local *c*-axis direction of the calcium carbonate material, while the intensity encodes the strength of the dichroism. The calcite shell PIC map shows needle-like prism structures, which are micron-size. Large single crystalline vaterite structures are visible in the spicule PIC map; these structures have dimensions exceeding 10 µm.

Biomineral samples are usually electrically insulating, and careful surface preparation is necessary to make them compatible with X-PEEM studies. A proven recipe is to embed small fragments or crystallites in epoxy, polish the sample surface to optical quality, and then differentially coat the flat surface with a noble metal, such as Pt [10.118]. A 1-nm-thick coating of Pt has been shown to be sufficient to prevent charging and is thin enough to allow the low-energy electrons that X-PEEM relies on to escape through the coating. Often, a thicker coating is deposited on the outer areas

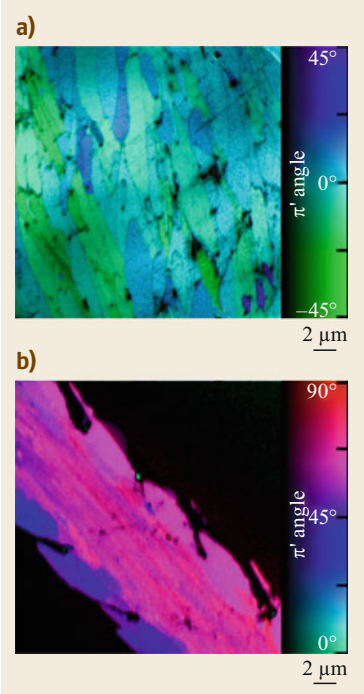

Fig. 10.22a,b Color PIC maps at the O K-edge of calcite and vaterite biominerals in cross-section with a 20-µm field of view. **(a)** Calcite prismatic layer in a *M. californianus* shell. The variations in color correspond to the distribution of calcite orientation angles. **(b)** Vaterite tunic spicule from the tunicate *Herdmania momus*. The homogeneous color indicates a common direction of the crystal across a large area of the spicule. The *color bars* to the *right* of each map show the strength of the dichroism and the angle relative to the linear x-ray polarization direction, which was in the plane of the sample. (Reprinted with permission from [10.117], copyright 2014 by the American Chemical Society) ◄

of the sample, which are not being imaged, to ensure a good electrical connection of the sample surface to the sample holder. Similar coating techniques have been successfully used on insulating metal oxides, e. g., NiO, and can also be relied on when studying air-sensitive samples that are not prepared in situ. Thin layers of Pd, Pt, Ta, or Al are frequently employed to prevent surface oxidization of reactive metals.

Modern PEEM microscopes that are equipped with an energy analyzer or electron spectrometer are frequently used for XPS and ARPES. Common designs use a hemispherical analyzer [10.120] or an omega filter [10.36], or utilize the dispersion of the magnetic beam separator of an aberration-corrected X-PEEM [10.121]. An energy resolution of better than 200 meV has been reached in microprobe XPS mode by selecting a region of the sample using an aperture placed in an image plane, or, alternatively, by using an imaging energy analyzer as a band-pass filter.

Some X-PEEM instruments that are equipped with an imaging energy filter can also be used for angle-resolved photoemission experiments by isolating the signal originating from a micron or sub-micron-size area of the sample using an image plane aperture and then imaging the angular distribution of the electron emission using the projector optics. For example, *Locatelli* et al. imaged the Fermi surface of graphene islands on Ir(001) [10.119] (Fig. 10.23). The X-PEEM intensity of the graphene is concentrated at Dirac points, at the K-point of the Brillouin zone of graphene. A dark field image, which was acquired by centering a contrast aperture on the K-point emission, shows a bright graphene-covered area on a dark substrate background. The au-

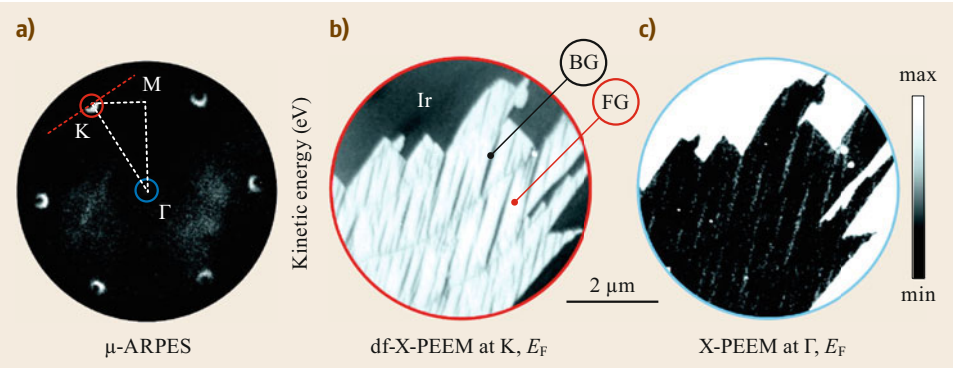

Fig. 10.23 **(a)** µ-ARPES measurement of the Fermi surface of a graphene island on Ir(001). X-PEEM images formed by electrons with momenta near the K-point **(b)** and near the Γ-point. **(c)** Two phases: a flat graphene phase, labeled FG, and a buckled phase, labeled BG. (Reprinted with permission from [10.119], copyright 2013 by the American Chemical Society)

thors observed that wrinkles in the graphene constitute a buckled phase. These buckled graphene (BG) regions appear darker than the flat graphene (FG) regions in the dark field image. They appear brighter in a so-called bright field image, which was taken with the contrast aperture centered on the Γ-point, which in this case corresponds to electrons emitted vertically from the sample and traveling along the optical axis of the microscope. Microscopes that are equipped with an imaging energy filter are ideal for photoemission studies that need speed and high spatial resolution, but only moderate energy resolution.

10.6 Time-Resolved Microscopy

Electron storage rings produce trains of x-ray pulses that can be used for stroboscopic measurements of time-dependent phenomena. Synchrotron x-ray pulses are typically between 30 and 100 ps in length. The temporal spacing between pulses depends on the fill pattern of the storage ring and usually lies between 1 and 1000 ns. Short and quickly repeated, periodic pulse trains are used for the study of non-stochastic, event-driven dynamics. Such repetitive pump–probe-style experiments use an initial *pump pulse*, for example, an electric pulse, a magnetic field pulse, or an optical pulse, to initiate a process, and then use a *probe pulse* to interrogate the state at a fixed delay time Δt, Fig. 10.24. The time evolution of the dynamics is then sampled with a time resolution corresponding to the x-ray pulse length by varying the delay between pump and probe pulse. Since the number of photons per x-ray pulse from a storage ring x-ray source is low, the signal from many probe pulses needs to be averaged. It is, therefore, necessary to reset the state of the sample after each probe pulse. This can be achieved either by waiting for the sample to relax into a unique ground state configuration or by actively switching the sample back to its original state using a reset pulse. Time-resolved imaging of magnetic domain dynamics is an important application of time-resolved X-PEEM [10.97, 98, 122–124].

10.6.1 Experimental Setup

We will describe a measurement technique developed at the ALS that relies on fast electric and magnetic pulses produced by an optical-laser-triggered photoconductive switch. Similar pulse generation techniques have been used and developed at several synchrotron radiation facilities [10.97, 122–124]. Switch, waveguide, and magnetic structures were integrated by photolithography and focused ion beam etching on a single semi-insulating GaAs. Electrical pulses were triggered by light pulses from a femtosecond titanium sapphire laser oscillator hitting an interdigitated, finger-like GaAs photoswitch. The laser was synchronized and phase locked to the synchrotron orbit and bunch clocks at a repetition frequency of 125 MHz. The magnetic structures were directly grown and patterned on top of the waveguide in a region where the generated magnetic field was in-plane, or parallel to the sample surface. A schematic drawing of the sample and experiment is shown in Fig. 10.25 [10.125].

10.6.2 In Situ Measurement of the Field Pulse

Electron imaging by X-PEEM is sensitive to small electric and magnetic fields, which means that X-PEEM can be used to record the temporal profile of the electric and magnetic field pulse. Figure 10.26a shows line profiles across a waveguide that are arranged by the

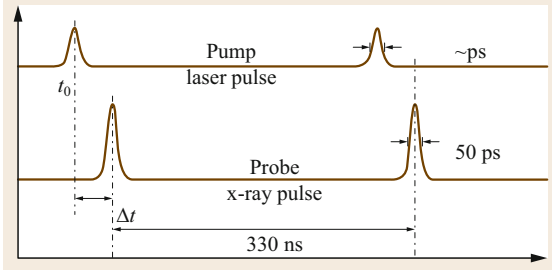

Fig. 10.24 Pulse sequence in a laser-synchrotron pump–probe experiment. A fast optical laser pulse excites the sample (pump), and an x-ray pulse probes the dynamic after a variable delay Δt

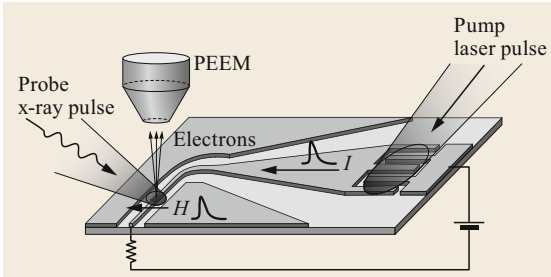

Fig. 10.25 Layout of the time-resolved PEEM experiment at the ALS. The laser triggers a photoconductive GaAs switch and generates a field pulse. The PEEM images the dynamics of the sample. (Reprinted with permission from [10.98], copyright 2004 by AAAS/Science)

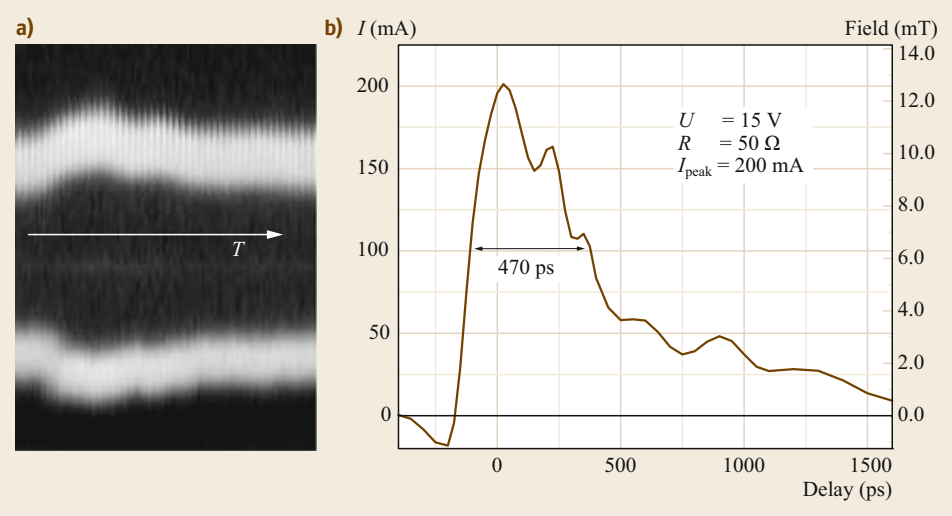

Fig. 10.26a,b X-PEEM records the field pulse by sensing the image distortion caused by the potential difference between waveguide and ground plane. A pulse with a fast rising edge and less than 500 ps in length was recorded. (Reprinted with permission from [10.125], copyright 2004 by the American Institute of Physics)

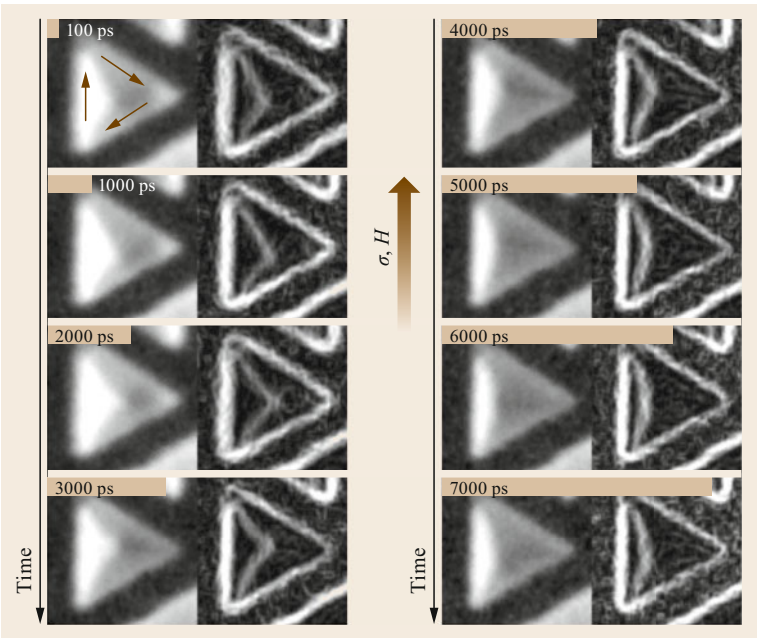

Fig. 10.27 Vortex dynamics in a triangular FeCo structure after an in-plane field pulse. Computed gradient images show domain walls with enhanced contrast. The *large brown arrow* shows the direction of the circular x-ray polarization and the magnetic field pulse, and the *small brown arrows* show the local direction of the magnetization in the vortex pattern

time delay T between the optical trigger launching the electrical pulse and the x-ray probe. Central wire and exterior ground planes of this coplanar waveguide appear dark in this image, while the gap between metallized layers appears bright. The apparent expansion of the electron optical image of the waveguide during the electrical pulse can be interpreted as being a result of the time-dependent electrical potential at the surface of the waveguide. The microscope works as an electric-field-sensing oscilloscope with 50-ps temporal resolution, the x-ray pulse length. The estimated current and the strength of the field pulse are plotted in Fig. 10.26b. This experiment showed a fast rising edge with a rise time comparable to the x-ray-pulse-limited temporal resolution of 50 ps, and a slower, approximately exponential decay that was modulated by some ringing due to reflections at the switch and the ground connection. The maximum current at 15 V switch bias

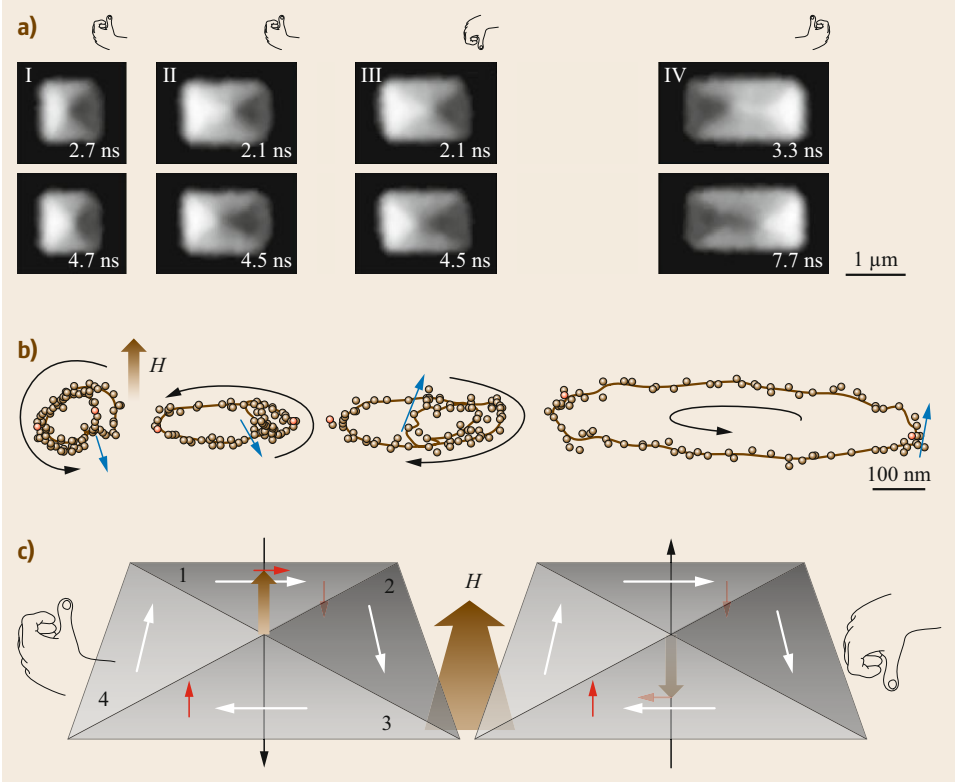

Fig. 10.28 **(a)** Domain images of the in-plane magnetization of pattern I ($1\times1\,\mu m^2$), patterns II and III ($1.5\times1\,\mu m^2$), and pattern IV ($2\times1\,\mu m^2$), taken at the specified delay times after the field pulse. The images are part of a time series extending over 8 ns and were chosen so that the horizontal displacement of the vortex has maximum amplitude. *Hands* illustrate the vortex handedness and the out-of-plane core magnetization as determined from the vortex dynamics. **(b)** Trajectories of the vortex core. *Dots* represent sequential vortex positions (100-ps step). **(c)** Spin structure of a left-handed (*left side*) and a right-handed (*right side*) square vortex. *Red arrows* represent the precessional torque generated by the external magnetic field (*brown arrow*). (Reprinted with permission from [10.98], copyright 2004 by AAAS/Science)

was about 200 mA, which corresponded to a peak field of 13 mT (130 Oe) directly on top of the center conductor of the waveguide.

10.6.3 Vortex Dynamics

Figure 10.27 shows a time sequence of PEEM XMCD images of a 2.5-μm-wide and 20-nm-thick, triangular soft-magnetic FeCo structure. The local direction of the magnetization is shown by arrows, which indicate that the ground state of the pattern is a magnetic vortex. A magnetic vortex is characterized by a curling magnetization that minimizes the magnetic stray field and has minimal dipolar energy. The center of the vortex is connected to the corners by three in-plane Neel domain walls. Two of these walls are well visible in processed images after applying a gradient filter. The train of field pulses, repeated at 125 MHz, causes a resonant precision of the central region of the pattern around the pattern center. For pulses that are well below 1 ns in duration, like in this experiment, the response of the magnetic structure is determined by precessional dynamics, while slower pulses respond by the process of magnetization damping. The images show this precessional, oscillating response of the magnetic pattern with a temporal resolution of 50 ps and a spatial resolution of better than 100 nm, which is sufficient to resolve the domain wall motion.

The dynamic response of several rectangular magnetic vortex structures is described in Fig. 10.28 [10.98]. Below the XMCD images, which are representative images for two delay times, the trajectory of the nanometer-size vortex core region is shown. All structures showed an initial acceleration of the core aligned with the magnetic field during the field pulse, followed by a field-free gyrotropic (spiraling) rotation of the vortex center around the center of the magnetic structure. Interestingly, when the trajectories of

patterns II and III were compared, different acceleration directions and rotation senses were observed in two patterns that appeared to have identical domain configurations. This was interpreted as being caused by a hidden parameter in the system: the perpendicular magnetization of the vortex core [10.126]. The perpendicular vortex core and the in-plane curling magnetization together formed a chiral system, which could be either right or left-handed. The handedness, or chirality, governed the field response and precessional dynamics of the system. A left-handed vortex was accelerated parallel to an applied field, whereas a right-handed vortex was accelerated antiparallel to the field, leading to new insight into the sub-nanosecond response of microscopic magnetic patterns to fast field pulses.

10.7 Conclusion

The X-PEEM technique combines the electronic and chemical sensitivity of x-ray spectroscopy and the high spatial resolution of electron imaging. It excels at surface imaging, exploiting the short mean free path of low-energy electrons. Time-resolved PEEM is only limited in temporal resolution by the duration of the probe pulse, and picosecond dynamic imaging of nanostructures has been demonstrated. New schemes of aberration correction push down the spatial resolution from 20–50 nm to only a few nanometers, making X-PEEM a core nanoscience technique that uses synchrotron radiation.

Acknowledgments. We would like to thank our collaborators E. Folven, Y. Takamura, J. Grepstad, A. Farhan, B. Leung, A.P. Hitchcock, and P.U.P.A. Gilbert, whose ALS work is discussed in this chapter. The chapter was copyedited by C.E. Scholl. This research used resources of the Advanced Light Source, which is a DOE Office of Science User Facility under contract no. DE-AC02-05CH11231.

References

10.1 E. Bauer: Low energy electron microscopy, Rep. Prog. Phys. **57**, 895–938 (1994)
10.2 A. Einstein: Über einen die Erzeugung und Verwandlung des Lichtes betreffenden heuristischen Gesichtspunkt, Ann. Phys. **17**, 132 (1905)
10.3 E. Brüche: Electron microscope image with photo-electrons, Z. Phys. **86**, 448–450 (1933)
10.4 E. Brüche, H. Johannson: Kinematographische Elektronenmikroskopie von Oxydkathoden, Ann. Phys. **407**, 145–166 (1932)
10.5 M. Knoll, F.G. Houtermans, W. Schulze: Untersuchung der Emissionsverteilung an Glühkathoden mit dem magnetischen Elektronenmikroskop, Z. Phys. **78**, 340–362 (1932)
10.6 D.B. Langmuir: Theoretical limitations of cathode-ray tubes, Proc. Inst. Radio Eng. **25**, 977–991 (1937)
10.7 A. Recknagel: Theorie des elektrischen Elektronenmikroskops für Selbststrahler, Z. Phys. **117**, 689–708 (1941)
10.8 W. Engel: Emission microscopy with different kinds of electron emission. In: *Proc. 6th Int. Congr. Electron Microsc., Kyoto, Japan* (Maruzen, Tokyo 1966)
10.9 L. Wegmann: Photoemission electron-microscope: its technique and applications, J. Microsc. **96**(1), 1–23 (1972)
10.10 O.H. Griffith, G.E. Rempfer: Photoelectron imaging: Photoelectron microscopy and related techniques, Adv. Opt. Electron Microsc. **10**, 269–337 (1987)
10.11 O.H. Griffith, W. Engel: Historical-perspective and current trends in emission microscopy, mirror electron-microscopy and low-energy electron-microscopy—An introduction to the Proceedings of the 2nd International-Symposium and Workshop on Emission Microscopy and Related Techniques, Ultramicroscopy **36**, 1–28 (1991)
10.12 E. Bauer: Surface electron-microscopy—The first 30 years, Surf. Sci. **299**, 102–115 (1994)
10.13 G.F. Rempfer, W.P. Skoczylas, O.H. Griffith: Design and performance of a high-resolution photoelectron microscope, Ultramicroscopy **36**, 196–221 (1991)
10.14 G.F. Rempfer: Unipotential electrostatic lenses—paraxial properties and aberrations of focal length and focal point, J. Appl. Phys. **57**, 2385–2401 (1985)
10.15 G.F. Rempfer, O.H. Griffith: The resolution of photoelectron microscopes with UV, X-ray, and synchrotron excitation sources, Ultramicroscopy **27**, 273–300 (1989)
10.16 W. Telieps, E. Bauer: An analytical reflection and emission UHV surface electron-microscope, Ultramicroscopy **17**, 57–65 (1985)
10.17 T. Schmidt, S. Heun, J. Slezak, J. Diaz, K.C. Prince, G. Lilienkamp, E. Bauer: SPELEEM: combining LEEM and spectroscopic imaging, Surf. Rev. Lett. **5**, 1287–1296 (1998)
10.18 B.P. Tonner, G.R. Harp: Photoelectron microscopy with synchrotron radiation, Rev. Sci. Instrum. **59**, 853–858 (1988)

10.19 J. Stöhr, Y. Wu, B.D. Hermsmeier, M.G. Samant, G.R. Harp, S. Koranda, D. Dunham, B.P. Tonner: Element-specific magnetic microscopy with circularly polarized X-rays, Science **259**, 658–661 (1993)

10.20 S. Anders, H.A. Padmore, R.M. Duarte, T. Renner, T. Stammler, A. Scholl, M.R. Scheinfein, J. Stöhr, L. Seve, B. Sinkovic: Photoemission electron microscope for the study of magnetic materials, Rev. Sci. Instrum. **70**, 3973–3981 (1999)

10.21 L.J. Heyderman, F. Nolting, C. Quitmann: X-ray photoemission electron microscopy investigation of magnetic thin film antidot arrays, Appl. Phys. Lett. **83**, 1797–1799 (2003)

10.22 W. Kuch, J. Gilles, F. Offi, S.S. Kang, S. Imada, S. Suga, J. Kirschner: Imaging microspectroscopy of Ni/Fe/Co/Cu(001) using a photoemission microscope, J. Electron Spectrosc. Relat. Phenom. **109**, 249–265 (2000)

10.23 C.M. Schneider, G. Schönhense: Investigating surface magnetism by means of photoexcitation electron emission microscopy, Rep. Prog. Phys. **65**, R1785–R1839 (2002)

10.24 D.H. Wei, Y.J. Hsu, R. Klauser, I.H. Hong, G.C. Yin, T.J. Chuang: Photoelectron microscopy projects at SRRC, Surf. Rev. Lett. **10**, 617–624 (2003)

10.25 F. Kronast, J. Schlichting, F. Radu, S.K. Mishra, T. Noll, H.A. Durr: Spin-resolved photoemission microscopy and magnetic imaging in applied magnetic fields, Surf. Interface Anal. **42**, 1532–1536 (2010)

10.26 T. Schmidt, U. Groh, R. Fink, E. Umbach: XPEEM with energy-filtering: Advantages and first results from the smart project, Surf. Rev. Lett. **9**, 223–232 (2002)

10.27 A. Doran, M. Church, T. Miller, G. Morrison, A.T. Young, A. Scholl: Cryogenic PEEM at the advanced light source, J. Electron Spectrosc. Relat. Phenom. **185**, 340–346 (2012)

10.28 A. Locatelli, L. Aballe, T.O. Mentes, M. Kiskinova, E. Bauer: Photoemission electron microscopy with chemical sensitivity: SPELEEM methods and applications, Surf. Interface Anal. **38**, 1554–1557 (2006)

10.29 X.M. Cheng, D.J. Keavney: Studies of nanomagnetism using synchrotron-based x-ray photoemission electron microscopy (X-PEEM), Rep. Prog. Phys. **75**, 026501 (2012)

10.30 L. Aballe, M. Foerster, E. Pellegrin, J. Nicolas, S. Ferrer: The ALBA spectroscopic LEEM-PEEM experimental station: layout and performance, J. Synchrotron Radiat. **22**, 745–752 (2015)

10.31 F.Z. Guo, T. Wakita, H. Shimizu, T. Matsushita, T. Yasue, T. Koshikawa, E. Bauer, K. Kobayashi: Introduction of photoemission electron microscopes at SPring-8 for nanotechnology support, J. Phys. Condens. Matter **17**, S1363–S1370 (2005)

10.32 R. Belkhou, S. Stanescu, S. Swaraj, A. Besson, M. Ledoux, M. Hajlaoui, D. Dalle: HERMES: A soft X-ray beamline dedicated to X-ray microscopy, J. Synchrotron Radiat. **22**, 968–979 (2015)

10.33 G. Salazar-Alvarez, J.J. Kavich, J. Sort, A. Mugarza, S. Stepanow, A. Potenza, H. Marchetto, S.S. Dhesi, V. Baltz, B. Dieny, A. Weber, L.J. Heyderman, J. Nogues, P. Gambardella: Direct evidence of imprinted vortex states in the antiferromagnet of exchange biased microdisks, Appl. Phys. Lett. **95**, 012510-3 (2009)

10.34 M. Haider, H. Rose, S. Uhlemann, B. Kabius, K. Urban: Towards 0.1 nm resolution with the first spherically corrected transmission electron microscope, J. Electron Microsc. **47**, 395–405 (1998)

10.35 G.F. Rempfer, D.M. Desloge, W.P. Skoczylas, O.H. Griffith: Simultaneous correction of spherical and chromatic aberrations with an electron mirror: An electron optical achromat, Microsc. Microanal. **3**, 14–27 (1997)

10.36 R. Fink, M.R. Weiss, E. Umbach, D. Preikszas, H. Rose, R. Spehr, P. Hartel, W. Engel, R. Degenhardt, R. Wichtendahl, H. Kuhlenbeck, W. Erlebach, K. Ihmann, R. Schlogl, H.J. Freund, A.M. Bradshaw, G. Lilienkamp, T. Schmidt, E. Bauer, G. Benner: SMART: A planned ultrahigh-resolution spectromicroscope for BESSY II, J. Electron Spectrosc. Relat. Phenom. **84**, 231–250 (1997)

10.37 P. Hartel, D. Preikszas, R. Spehr, H. Müller, H. Rose: Mirror corrector for low-voltage electron microscopes. In: *Advances in Imaging and Electron Physics*, Vol. 120, ed. by P. Hawkes (Elsevier, Amsterdam 2003) pp. 41–133

10.38 R.M. Tromp, J.B. Hannon, A.W. Ellis, W. Wan, A. Berghaus, O. Schaff: A new aberration-corrected, energy-filtered LEEM/PEEM instrument. I. Principles and design, Ultramicroscopy **110**, 852–861 (2010)

10.39 R. Konenkamp, R.C. Word, G.F. Rempfer, T. Dixon, L. Almaraz, T. Jones: 5.4 nm spatial resolution in biological photoemission electron microscopy, Ultramicroscopy **110**, 899–902 (2010)

10.40 J. Feng, E. Forest, A.A. MacDowell, M. Marcus, H. Padmore, S. Raoux, D. Robin, A. Scholl, R. Schlueter, P. Schmid, J. Stohr, W. Wan, D.H. Wei, Y. Wu: An x-ray photoemission electron microscope using an electron mirror aberration corrector for the study of complex materials, J. Phys. Condens. Matter **17**, S1339–S1350 (2005)

10.41 D.T. Attwood: *Soft x-rays and extreme ultraviolet radiation: principles and applications* (Cambridge Univ. Press, Cambridge 2000)

10.42 B.P. Tonner, D. Dunham: Sub-micron spatial resolution of a micro-XAFS electrostatic microscope with bending magnet radiation: performance assessments and prospects for aberration correction, Nucl. Instrum. Methods Phys. Res. A **347**, 436–440 (1994)

10.43 R. Nakajima, J. Stohr, Y.U. Idzerda: Electron-yield saturation effects in L-edge X-ray magnetic circular dichroism spectra of Fe, Co, and Ni, Phys. Rev. B **59**, 6421–6429 (1999)

10.44 H. Ohara, Y. Yamamoto, K. Kajikawa, H. Ishii, K. Seki, Y. Ouchi: Effective escape depth of photoelectrons for hydrocarbon films in total electron yield measurement at the C K-edge, J. Synchrotron Radiat. **6**, 803–804 (1999)

10.45 M. Zharnikov, S. Frey, K. Heister, M. Grunze: An extension of the mean free path approach to X-ray absorption spectroscopy, J. Electron Spectrosc. Relat. Phenom. **124**, 15–24 (2002)

10.46 J. Lüning, F. Nolting, A. Scholl, H. Ohldag, J.W. Seo, J. Fompeyrine, J.P. Locquet, J. Stöhr: Determination of the antiferromagnetic spin axis in epitaxial $LaFeO_3$ films by x-ray magnetic linear dichroism spectroscopy, Phys. Rev. B **67**, 214433 (2003)

10.47 M. Marcus: The effect of sample tilt on an emission microscope, Surf. Sci. **480**, 203–207 (2001)

10.48 S.A. Nepijko, N.N. Sedov, G. Schönhense, M. Escher, X. Bao, W. Huang: Resolution deterioration in emission electron microscopy due to object roughness, Ann. Phys. **9**, 441–451 (2000)

10.49 J. Stöhr: *NEXAFS Spectroscopy*, Vol. 25 (Springer, Berlin 1992)

10.50 S.G. Urquhart, A.P. Hitchcock, A.P. Smith, H.W. Ade, W. Lidy, E.G. Rightor, G.E. Mitchell: NEXAFS spectromicroscopy of polymers: overview and quantitative analysis of polyurethane polymers, J. Electron Spectrosc. Relat. Phenom. **100**, 119–135 (1999)

10.51 J. Chmelik, L. Veneklasen, G. Marx: Comparing cathode lens configurations for low energy electron microscopy, Optik **83**, 155–160 (1989)

10.52 E. Harting, F. Read: *Electrostatic Lenses* (Elsevier, Amsterdam 1976)

10.53 P. Hawkes: *Image Processing and Computer-Aided Design in Electron Optics* (Academic Press, New York 1973)

10.54 J. Orloff: *Handbook of Charged Particle Optics* (CRC, Boca Raton 1997)

10.55 J. Zlamal, B. Lencova: Development of the program EOD for design in electron and ion microscopy, Nucl. Instrum. Methods Phys. Res. A **645**, 278–282 (2011)

10.56 D.A. Dahl: SIMION for the personal computer in reflection, Int. J. Mass Spectrom. **200**, 3–25 (2000)

10.57 C.J. Davisson, C.J. Calbick: Electron lenses, Phys. Rev. **42**, 0580 (1932)

10.58 R.N. Watts, S. Liang, Z.H. Levine, T.B. Lucatorto, F. Polack, M.R. Scheinfein: A transmission X-ray microscope based on secondary-electron imaging, Rev. Sci. Instrum. **68**, 3464–3476 (1997)

10.59 B. Lencova: Electrostatic lenses. In: *Handbook of Charged Particle Optics*, 2nd edn., ed. by J. Orloff (CRC, Boca Raton 2008) pp. 161–208

10.60 E. Bauer: The possibilities for analytical methods in photoemission and low-energy microscopy, Ultramicroscopy **36**, 52–62 (1991)

10.61 G. Schneider: Cryo X-ray microscopy with high spatial resolution in amplitude and phase contrast, Ultramicroscopy **75**, 85–104 (1998)

10.62 C. Jacobsen, J. Kirz, S. Williams: Resolution in soft X-ray microscopes, Ultramicroscopy **47**, 55–79 (1992)

10.63 J. Feng, H. Padmore, D.H. Wei, S. Anders, Y. Wu, A. Scholl, D. Robin: Modeling the acceleration field and objective lens for an aberration corrected photoemission electron microscope, Rev. Sci. Instrum. **73**, 1514–1517 (2002)

10.64 H. Rose: Correction of aberrations, a promising means for improving the spatial and energy resolution of energy-filtering electron microscopes, Ultramicroscopy **56**, 11–25 (1994)

10.65 O. Scherzer: Over some errors of electrons lenses, Z. Phys. **101**, 593–603 (1936)

10.66 P.W. Hawkes, E. Kasper: *Principles of Electron Optics*, Vol. 2 (Academic Press, New York 1996)

10.67 J. Zach, M. Haider: Correction of spherical and chromatic aberration in a low voltage SEM, Optik **98**, 112–118 (1995)

10.68 M. Haider, H. Rose, S. Uhlemann, E. Schwan, B. Kabius, K. Urban: A spherical-aberration-corrected 200 kV transmission electron microscope, Ultramicroscopy **75**, 53–60 (1998)

10.69 M. Haider, S. Uhlemann, E. Schwan, H. Rose, B. Kabius, K. Urban: Electron microscopy image enhanced, Nature **392**, 768–769 (1998)

10.70 N. Dellby, O.L. Krivanek, P.D. Nellist, P.E. Batson, A.R. Lupini: Progress in aberration-corrected scanning transmission electron microscopy, J. Electron Microsc. **50**, 177–185 (2001)

10.71 P.E. Batson, N. Dellby, O.L. Krivanek: Sub-ångstrom resolution using aberration corrected electron optics, Nature **418**, 617–620 (2002)

10.72 G. De Stasio, L. Perfetti, B. Gilbert, O. Fauchoux, M. Capozi, P. Perfetti, G. Margaritondo, B.P. Tonner: MEPHISTO spectromicroscope reaches 20 nm lateral resolution, Rev. Sci. Instrum. **70**, 1740–1742 (1999)

10.73 E. Bauer: *Chemical, Structural, and Electronic Analysis of Heterogeneous Surfaces on Nanometer Scale* (Kluwer, Dortrecht 1997)

10.74 G. Schönhense, H. Spiecker: Correction of chromatic and spherical aberration in electron microscopy utilizing the time structure of pulsed excitation sources, J. Vac. Sci. Technol. B **20**, 2526–2534 (2002)

10.75 E. Bauer: Photoelectron spectromicroscopy: present and future, J. Electron Spectrosc. Relat. Phenom. **114–116**, 975–987 (2001)

10.76 V.K. Zworykin, V. Kosma: *Electron Optics and the Electron Microscope* (Wiley, New York 1945)

10.77 E.G. Ramberg: Aberration correction with electron mirrors, J. Appl. Phys. **20**, 183–186 (1949)

10.78 V.M. Kel'man, L.M. Sekunova, E.M. Yakushev: Theory of axisymmetric electron mirrors I. Trajectory equations, Sov. Phys. Tech. Phys. **17**, 2279 (1973)

10.79 V.M. Kel'man, L.M. Sekunova, E.M. Yakushev: Theory of axisymmetric electron mirrors. I. Trajectory equations, Sov. Phys. Tech. Phys. **18**, 1142 (1974)

10.80 A.L. Dodin, M.B. Nesvizhskii: Accuracy of expansions in deriving the geometric aberration coefficients of cathode systems, Sov. Phys. Tech. Phys. **26**, 539–541 (1981)

10.81 G.F. Rempfer: A theoretical study of the hyperbolic electron mirror as a correcting element for spherical and chromatic aberration in electron optics, J. Appl. Phys. **67**, 6027–6040 (1990)

10.82 G.F. Rempfer, M.S. Mauck: Correction of chromatic aberration with an electron mirror, Optik **92**, 3–8 (1992)

10.83 G.F. Rempfer, D.M. Desloge, W.P. Skoczylas, O. Hayes Griffith: Simultaneous correction of spherical and chromatic aberrations with an electron mirror: An electron optical achromat, Microsc. Microanal. **3**, 14–27 (1997)

10.84 Z. Shao, X.D. Wu: Properties of a four-electrode adjustable electron mirror as an aberration corrector, Rev. Sci. Instrum. **61**, 1230–1235 (1990)

10.85 Z. Shao, X.D. Wu: A study on hyperbolic mirrors as correctors, Optik **84**, 51–54 (1990)

10.86 H. Rose, D. Preikszas: Time-dependent perturbation formalism for calculating the aberrations of systems with large ray gradients, Nucl. Instrum. Methods Phys. Res. A **363**, 301–315 (1995)

10.87 D. Preikszas, H. Rose: Correction properties of electron mirrors, J. Electron Microsc. **46**, 1–9 (1997)

10.88 H. Rose, D. Preikszas: Outline of a versatile corrected LEEM, Optik **92**, 31–44 (1992)

10.89 W. Wan, J. Feng, H.A. Padmore, D.S. Robin: Simulation of a mirror corrector for PEEM3, Nucl. Instrum. Methods Phys. Res. A **519**, 222 (2004)

10.90 W. Wan, J. Feng, H.A. Padmore: A new separator design for aberration corrected photoemission electron microscopes, Nucl. Instrum. Methods Phys. Res. A **564**, 537–543 (2006)

10.91 J. Feng, A.A. MacDowell, R. Duarte, A. Doran, E. Forest, N. Kelez, M. Marcus, D. Munson, H. Padmore, K. Petermann, S. Raoux, D. Robin, A. Scholl, R. Schlueter, P. Schmid, J. Stohr, W. Wan, D.H. Wei, Y. Wu: An aberration corrected photoemission electron microscope at the advanced light source, AIP Conf. Proc. **705**, 1070–1073 (2004)

10.92 F. Nolting, A. Scholl, J. Stöhr, J.W. Seo, J. Fompeyrine, H. Siegwart, J.P. Locquet, S. Anders, J. Lüning, E.E. Fullerton, M.F. Toney, M.R. Scheinfein, H.A. Padmore: Direct observation of the alignment of ferromagnetic spins by antiferromagnetic spins, Nature **405**, 767–769 (2000)

10.93 J.B. Kortright, D.D. Awschalom, J. Stöhr, S.D. Bader, Y.U. Idzerda, S.S.P. Parkin, I.K. Schuller, H.C. Siegmann: Research frontiers in magnetic materials at soft X-ray synchrotron radiation facilities, J. Magn. Magn. Mater. **207**, 7–44 (1999)

10.94 G. Schütz, W. Wagner, W. Wilhelm, P. Kienle, R. Zeller, R. Frahm, G. Materlik: Absorption of circularly polarized X rays in iron, Phys. Rev. Lett. **58**, 737–740 (1987)

10.95 J. Stöhr, A. Scholl, T.J. Regan, S. Anders, J. Lüning, M.R. Scheinfein, H.A. Padmore, R.L. White: Images of the antiferromagnetic structure of a NiO(100) surface by means of X-ray magnetic linear dichroism spectromicroscopy, Phys. Rev. Lett. **83**, 1862–1865 (1999)

10.96 A. Scholl, J. Stöhr, J. Lüning, J.W. Seo, J. Fompeyrine, H. Siegwart, J.P. Locquet, F. Nolting, S. Anders, E.E. Fullerton, M.R. Scheinfein, H.A. Padmore: Observation of antiferromagnetic domains in epitaxial thin films, Science **287**, 1014–1016 (2000)

10.97 J. Vogel, W. Kuch, M. Bonfim, J. Camarero, Y. Pennec, F. Offi, K. Fukumoto, J. Kirschner, A. Fontaine, S. Pizzini: Time-resolved magnetic domain imaging by x-ray photoemission electron microscopy, Appl. Phys. Lett. **82**, 2299–2301 (2003)

10.98 S.B. Choe, Y. Acremann, A. Scholl, A. Bauer, A. Doran, J. Stohr, H.A. Padmore: Vortex core-driven magnetization dynamics, Science **304**, 420–422 (2004)

10.99 B.T. Thole, C. Paolo, F. Sette, G. van der Laan: X-ray circular dichroism as a probe of orbital magnetization, Phys. Rev. Lett. **68**, 1943–1946 (1992)

10.100 Y. Wu, J. Stohr, B.D. Hermsmeier, M.G. Samant, D. Weller: Enhanced orbital magnetic moment on Co atoms in Co/Pd multilayers: A magnetic circular X-ray dichroism study, Phys. Rev. Lett. **69**, 2307–1310 (1992)

10.101 P. Carra, B.T. Thole, M. Altarelli, W. Xindong: X-ray circular dichroism and local magnetic fields, Phys. Rev. Lett. **70**, 694–697 (1993)

10.102 P. Kuiper, B.G. Searle, P. Rudolf, L.H. Tjeng, C.T. Chen: X-ray magnetic dichroism of antiferromagnet Fe_2O_3: the orientation of magnetic moments observed by Fe 2p X-ray absorption spectroscopy, Phys. Rev. Lett. **70**, 1549–1552 (1993)

10.103 D. Alders, L.H. Tjeng, F.C. Voogt, T. Hibma, G.A. Sawatzky, C.T. Chen, J. Vogel, M. Sacchi, S. Iacobucci: Temperature and thickness dependence of magnetic moments in NiO epitaxial films, Phys. Rev. B **57**, 11623–11631 (1998)

10.104 E. Arenholz, G. van der Laan, R.V. Chopdekar, Y. Suzuki: Angle-dependent Ni^{2+}x-ray magnetic linear dichroism: interfacial coupling revisited, Phys. Rev. Lett. **98**, 197201-4 (2007)

10.105 H. Ohldag, T.J. Regan, J. Stöhr, A. Scholl, F. Nolting, J. Luning, C. Stamm, S. Anders, R.L. White: Spectroscopic identification and direct imaging of interfacial magnetic spins, Phys. Rev. Lett. **87**, 247201 (2001)

10.106 H. Ohldag, A. Scholl, F. Nolting, E. Arenholz, S. Maat, A.T. Young, M. Carey, J. Stöhr: Correlation between exchange bias and pinned interfacial spins, Phys. Rev. Lett. **91**, 017203 (2003)

10.107 E. Folven, A. Scholl, A. Young, S. Retterer, J. Boschker, T. Tybell, Y. Takamura, J. Grepstad: Crossover from spin-flop coupling to collinear spin alignment in antiferromagnetic/ferromagnetic nanostructures, Nano Lett. **12**, 2386–2390 (2012)

10.108 E. Folven, J. Linder, O. Gomonay, A. Scholl, A. Doran, A. Young, S. Retterer, V. Malik, T. Tybell, Y. Takamura, J. Grepstad: Controlling the switching field in nanomagnets by means of domain-engineered antiferromagnets, Phys. Rev. B **92**, 057204-5 (2013)

10.109 M.S. Lee, T.A. Wynn, E. Folven, R.V. Chopdekar, A. Scholl, A.T. Young, S.T. Retterer, J.K. Grepstad, Y. Takamura: Tailoring spin textures in complex oxide micromagnets, ACS Nano **10**, 8545–8551 (2016)

10.110 A. Farhan, P. Derlet, A. Kleibert, A. Balan, R. Chopdekar, M. Wyss, J. Perron, A. Scholl, F. Nolt-

ing, L. Heyderman: Direct observation of thermal relaxation in artificial spin ice, Phys. Rev. Lett. **111**, 197201–4 (2007)
10.111 I. Gilbert, Y.Y. Lao, I. Carrasquillo, L. O'Brien, J.D. Watts, M. Manno, C. Leighton, A. Scholl, C. Nisoli, P. Schiffer: Emergent reduced dimensionality by vertex frustration in artificial spin ice, Nature Phys. **12**, 162–165 (2016)
10.112 F. Kronast, N. Friedenberger, K. Ollefs, S. Gliga, L. Tati-Bismaths, R. Thies, A. Ney, R. Weber, C. Hassel, F.M. Romer, A.V. Trunova, C. Wirtz, R. Hertel, H.A. Durr, M. Farle: Element-specific magnetic hysteresis of individual 18 nm Fe nanocubes, Nano Lett. **11**, 1710–1715 (2011)
10.113 B. Leung, A. Hitchcock, R. Cornelius, J. Brash, A. Scholl, A. Doran: X-ray spectromicroscopy study of protein adsorption to a polystyrene-polylactide blend, Biomacromolecules **10**, 1838–1845 (2009)
10.114 I.N. Koprinarov, A.P. Hitchcock, C.T. McCrory, R.F. Childs: Quantitative mapping of structured polymeric systems using singular value decomposition analysis of soft X-ray images, J. Phys. Chem. B **106**, 5358–5364 (2002)
10.115 R.A. Metzler, M. Abrecht, R.M. Olabisi, D. Ariosa, C.J. Johnson, B.H. Frazer, S.N. Coppersmith, P.U.P.A. Gilbert: Architecture of columnar nacre, implications for its formation mechanism, Phys. Rev. Lett. **98**, 268102–4 (2007)
10.116 P.U.P.A. Gilbert, R.A. Metzler, D. Zhou, A. Scholl, A. Doran, A. Young, M. Kunz, N. Tamura, S.N. Coppersmith: Gradual ordering in red abalone nacre, J. Am. Chem. Soc. **130**, 17519–17527 (2008)
10.117 R.T. DeVol, R.A. Metzler, L. Kabalah-Amitai, B. Pokroy, Y. Politi, A. Gal, L. Addadi, S. Weiner, A. Fernandez-Martinez, R. Demichelis, J.D. Gale, J. Ihli, F.C. Meldrum, A.Z. Blonsky, C.E. Killian, C.B. Salling, A.T. Young, M.A. Marcus, A. Scholl, A. Doran, C. Jenkins, H.A. Bechtel, P.U.P.A. Gilbert: Oxygen spectroscopy and polarization-dependent imaging contrast (PIC)-mapping of calcium carbonate minerals and biominerals, J. Phys. Chem. B **118**, 8449–8457 (2014)
10.118 G. De Stasio, B.H. Frazer, B. Gilbert, K.L. Richter, J.W. Valley: Compensation of charging in X-PEEM: A successful test on mineral inclusions in 4.4 Ga old zircon, Ultramicroscopy **98**, 57–62 (2003)
10.119 A. Locatelli, C. Wang, C. Africh, N. Stojic, T.O. Mentes, G. Comelli, N. Binggeli: Temperature-driven reversible rippling and bonding of a graphene super lattice, ACS Nano **7**, 6955–6963 (2013)
10.120 M. Escher, N. Weber, M. Merkel, C. Ziethen, P. Bernhard, G. Schonhense, S. Schmidt, F. Forster, F. Reinert, B. Kromker, D. Funnemann: Nanoelectron spectroscopy for chemical analysis: A novel energy filter for imaging x-ray photoemission spectroscopy, J. Phys. Condens. Matter **17**, S1329–S1338 (2005)
10.121 R.M. Tromp, Y. Fujikawa, J.B. Hannon, A.W. Ellis, A. Berghaus, O. Schaff: A simple energy filter for low energy electron microscopy/photoelectron emission microscopy instruments, J. Phys. Condens. Matter **21**, 314007 (2009)
10.122 H. Stoll, A. Puzic, B. van Waeyenberge, P. Fischer, J. Raabe, M. Buess, T. Haug, R. Hollinger, C. Back, D. Weiss, G. Denbeaux: High-resolution imaging of fast magnetization dynamics in magnetic nanostructures, Appl. Phys. Lett. **84**, 3328–3330 (2004)
10.123 C.M. Schneider, A. Kuksov, A. Krasyuk, A. Oelsner, D. Neeb, S.A. Nepijko, G. Schonhense, I. Monch, R. Kaltofen, J. Morais, C. de Nadai, N.B. Brookes: Incoherent magnetization rotation observed in subnanosecond time-resolving x-ray photoemission electron microscopy, Appl. Phys. Lett. **85**, 2562–2564 (2004)
10.124 C. Quitmann, J. Raabe, C. Buehler, M. Buess, S. Johnson, F. Nolting, V. Schlott, A. Streun: Measuring magnetic excitations in microstructures using X-ray microscopy, Nucl. Instrum. Methods Phys. Res. A **588**, 494–501 (2008)
10.125 S.B. Choe, Y. Acremann, A. Bauer, A. Scholl, A. Doran, J. Stohr, H.A. Padmore: P-sec time-resolved microscopy of magnetic structures using X-PEEM, AIP Conf. Proc. **705**, 1391–1394 (2004)
10.126 T. Shinjo, T. Okuno, R. Hassdorf, K. Shigeto, T. Ono: Magnetic vortex core observation in circular dots of permalloy, Science **289**, 930–932 (2000)

Jun Feng

Advanced Light Source
Lawrence Berkeley National Laboratory
Berkeley, CA, USA
fjun@lbl.gov

Jun Feng received his PhD from the Institute of Modern Physics of the Chinese Academy of Science in 1991. He has worked at Shanghai Institute of Applied Physics, RIKEN, and the Lawrence Berkeley National Laboratory. He now works on novel energy materials, photocathode materials for high brightness electron beams, ultrafast science, high-resolution electron microscopy, synchrotron radiation instruments, and applications.

Andreas Scholl

Advanced Light Source
Lawrence Berkeley National Laboratory
Berkeley, CA, USA
a_scholl@lbl.gov

Andreas Scholl received his PhD from the University of Cologne and the Jülich Research Center. He works at LBNL's Advanced Light Source, a synchrotron facility that provides users from around the world access to the brightest beams of soft x-rays. He uses x-ray photoemission electron microscopy for the study of the magnetic, electronic, and chemical structure of materials.